A NEUROPROSTHESIS THAT ALLEVIATES LOCOMOTOR DEFICITS DUE TO PARKINSON'S DISEASE

Tomislav Milekovic[1,2,3,4,5,*], Eduardo Martin Moraud[2,3,4,*], Nicolo Macellari[1,2,3,4,&], Charlotte Moerman[2,3,4,&], Flavio Raschellà[1,6,&], Shiqi Sun[1,2,3,4,&], Matthew G. Perich[5,&], Camille Varescon[1,2,3,4], Robin Demesmaeker[1,2,3,4], Alice Bruel[7], Léa N. Bole-Feysot[1,2,3,4], Giuseppe Schiavone[1,8], Elvira Pirondini[2,3,21,23], Cheng YunLong[9,10], Li Hao[9,10], Andrea Galvez[1,2,3,4], Sergio Daniel Hernandez-Charpak[1,2,3,4], Gregory Dumont[1,2,3,4], Jimmy Ravier[1,2,3,4], Camille G. Le Goff-Mignardot[1,2,3,4], Jean-Baptiste Mignardot[1,2,3,4], Gaia Carparelli[1,2,3,4], Cathal Harte[1,2,3,4], Nicolas Hankov[1,2,3,4], Viviana Aureli[1,2,3,4], Anne Watrin[11], Hendrik Lambert[11], David Borton[1,2,3,4,12], Jean Laurens[1,13], Isabelle Vollenweider[1,2,3,4], Simon Borgognon[1,2,3,4], François Bourre[14,15], Michel Goillandeau[14,15], Wai Kin D Ko[9,10], Laurent Petit[14,15], Qin Li[7,8], Rik Buschman[16], Nicholas Buse[16], Maria Yaroshinsky[17], Jean-Baptiste Ledoux[18], Fabio Becce[18], Mayté Castro Jimenez[19], Julien F. Bally[19], Timothy Denison[20], Dominique Guehl[14,15], Auke Ijspeert[7], Marco Capogrosso[1,2,3,4,21], Jordan Squair[1,2,3,4], Leonie Asboth[1,2,3,4], Philip A. Starr[17], Doris D. Wang[17], Stéphanie P. Lacour[1,8], Silvestro Micera[1,6,22], Chuan Qin[10], Jocelyne Bloch[1,2,3,4,#,✉], Erwan Bezard[9,10,14,15,#,✉] and G. Courtine[1,2 3,4,#,✉]

[1] NeuroX Institute, School of Life Sciences, Ecole Polytechnique Fédérale de Lausanne (EPFL), Geneva, Switzerland,

[2] Department of Clinical Neurosciences, Lausanne University Hospital (CHUV) and University of Lausanne (UNIL), Lausanne, Switzerland,

[3] .NeuroRestore, Defitech Center for Interventional Neurotherapies, EPFL/CHUV/UNIL, Lausanne, Switzerland,

[4] Department of Neurosurgery, CHUV, Lausanne, Switzerland,

[5] Department of Fundamental Neuroscience, Faculty of Medicine, University of Geneva, Geneva, Switzerland,

[6] Bertarelli Foundation Chair in Translational Neuroengineering, NeuroX Institute, School of Bioengineering, EPFL, Lausanne, Switzerland,

[7] Institute of Bioengineering, School of Engineering, EPFL, Lausanne, Switzerland,

[8] Laboratory for Soft Bioelectronic Interfaces (LSBI), NeuroX Institute, EPFL, Switzerland,

[9] Motac Neuroscience, UK-M15 6WE, Manchester, United Kingdom and Institute of Laboratory Animal Sciences,

[10] China Academy of Medical Sciences, Beijing City, People's Republic of China,

[11] ONWARD medical, Lausanne, Switzerland,

[12] School of Engineering, Carney Institute for Brain Science, Brown University, Providence RI, 02912 USA,

[13] Department of Neuroscience, Baylor College of Medicine, Houston, TX, USA,

[14] Université de Bordeaux, Institut des Maladies Neurodégénératives, UMR 5293, F-33000 Bordeaux, France,

[15] CNRS, Institut des Maladies Neurodégénératives, UMR 5293, F-33000 Bordeaux, France,

[16] Medtronic, Minneapolis, USA,

[17] Department of Neurological Surgery, University of California, San Francisco, San Francisco, CA, USA,

[18] Department of Diagnostic and Interventional Radiology, CHUV/UNIL, Lausanne, Switzerland,

[19] Department of Neurology, CHUV/UNIL, Lausanne, Switzerland,

[20] Oxford University, Oxford, England,

[21] Rehab and Neural Engineering Labs, University of Pittsburgh, Pittsburgh, PA, USA,

[22] Department of Excellence in Robotics and AI, Biorobotics Institute, Scuola Superiore Sant'Anna, Pisa, Italy,

[23] Department of Physical Medicine and Rehabilitation, University of Pittsburgh, Pittsburgh, PA, USA,

* These authors contributed equally,

& These authors contributed equally,

# These authors jointly supervised this work.

✉ e-mail: erwan.bezard@u-bordeaux.fr, jocelyne.bloch@chuv.ch, gregoire.courtine@epfl.ch

ABSTRACT

People with late-stage Parkinson's disease (PD) often suffer from debilitating locomotor deficits that are resistant to currently available therapies. To alleviate these deficits, we developed a neuroprosthesis operating in closed-loop that targets the dorsal root entry zones innervating lumbosacral segments in order to modulate the regions of the spinal cord producing locomotion. We first developed this neuroprosthesis in a nonhuman primate (NHP) model that replicates locomotor deficits due to PD. We configured the neuroprosthesis to reproduce the natural spatiotemporal activation of the lumbosacral spinal cord during walking. This neuroprosthesis not only alleviated locomotor deficits but also restored skilled walking in NHPs. We then found that the neuroprosthesis interacted synergistically with deep brain stimulation of the subthalamic nucleus and dopaminergic replacement therapies to alleviate gait impairments, remedy balance problems and reduce freezing-of-gait in a person with PD. This neuroprosthesis opens new perspectives to reduce the severity of locomotor deficits in people with PD.

About 40% of people with PD experience locomotor deficits that include gait impairments, balance problems and freezing-of-gait episodes[1]. For people with late-stage PD, the prevalence of locomotor deficits rises to more than 90%[2]. These deficits severely reduce quality of life and increase comorbid conditions[3]. Unfortunately, these deficits respond poorly to currently available therapies, such as dopamine replacement strategies and deep brain stimulation (DBS) of the subthalamic nucleus[4-8]. These therapies often improve certain features of gait patterns, but have limited impact on dopa-resistant components such as gait initiation, balance, postural instability, and freezing-of-gait[7]. Indeed, the frequency and severity of freezing-of-gait episodes can even increase when DBS is turned on[7]. An alternative strategy involves the delivery of continuous electrical spinal cord stimulation over the cervical or thoracic segments of the spinal cord[9-14]. This stimulation aims to recruit ascending afferent fibers nested in the dorsal columns to modulate the activity of the basal ganglia and cerebral cortex[15,16]. Despite a reduction of locomotor deficits in some people with PD, the broader application of this strategy led to variable and unsatisfying outcomes[17-19]. Consequently, the identification of complementary therapies to alleviate locomotor deficits is defined as a priority for people with late-stage PD[7].

While currently available therapies focus on the neuronal circuits in the brain that are directly affected by the loss of dopamine-producing cells, an alternative strategy may instead target the neuronal circuits in the lumbosacral spinal cord that ultimately produce walking, and are *a priori* not directly affected by PD. We thus hypothesized that strategies capable of modulating the activity of the neuronal circuits in the lumbosacral spinal cord may be effective to alleviate locomotor deficits due to PD.

We previously showed that targeted epidural electrical stimulation (EES) of the lumbosacral spinal cord modulates the activity of motor neurons through the activation of large-diameter afferents where they enter the spinal cord through the dorsal root entry zones[20,21]. This physiological principle enables real-time control over the activity of leg motor neurons. Concretely, the individual dorsal root entry zones innervating lumbosacral segments are targeted with a precise timing that reproduces the natural spatiotemporal activation pattern of leg motor neurons[22,23]. This strategy restored standing, walking, cycling, and even swimming in people with paralysis due to spinal cord injury[24-26]. We reasoned that this strategy can be adapted to the specific context of PD to conceive a neuroprosthesis that alleviates locomotor deficits due to PD.

Preclinical model of PD showing locomotor deficits detected in people with PD

We aimed to develop a neuroprosthesis based on EES to alleviate gait impairments and balance problems due to PD. This development required establishing a preclinical model that replicates the key components of gait impairments and balance problems observed in humans with PD. The rhesus monkey treated with 1–methyl–4–phenyl–1,2,3,6–tetrahydropyridine (MPTP) is the most established preclinical model of PD[27]. However, the locomotor deficits of MPTP-treated NHPs have not yet been characterized with high-precision kinematic analyses. Therefore, it remains unclear whether the deficits observed during quadrupedal locomotion in MPTP-treated NHPs resemble those observed during the bipedal gait of people with PD.

To enable this comparison, we established comparable gait recording platforms for NHPs and humans that allowed high-resolution recordings of whole-body kinematics during natural locomotion in both species[28] (**Fig 1** and **Supplementary Movie 1**).

We first recorded locomotion in 9 rhesus monkeys before and after an MPTP treatment that modeled a late-stage of Parkinsonism (**Fig 1a-c**). This neurological stage coincided with the severe depletion of striatal dopaminergic terminals and nigral neurons (**Extended Data Fig. 1a**). We calculated an ensemble of kinematic variables that captured the key features of gait (**Supplementary Table 3**). We then implemented principal component (PC) analysis as an unbiased method to score locomotor performance and identify the more prominent variables to account for gait impairments[29]. PC1 and PC3 segregated gait patterns quantified before versus after MPTP treatment (**Fig. 1d**). Extraction of variables with the highest correlation with PC1 revealed that MPTP led to reduced stride length and slow movements ($p < 0.05$; **Extended Data Fig. 1a-b**). PC3 identified excessively flexed postures and impairments of trunk movements ($p < 0.01$; **Extended Data Fig. 1a-b**).

We next asked whether people with PD exhibited similar locomotor deficits. For this purpose, we quantified gait patterns of 25 people with PD whose neurological status covered a broad spectrum of impairments (**Supplementary Table 4**) and 9 healthy age-matched people **(Fig 1e-g)**. PC analysis applied on kinematic variables (**Supplementary Table 5**) revealed that the majority of gait impairments and balance problems observed in MPTP-treated NHPs were comparable to those quantified in our cohort of people with PD (**Fig. 1h** and **Extended Data Fig. 1d**).

These results show that MPTP–treated NHPs, classified with late-stage Parkinsonism based on neuronal loss and overall behavioral deficits, displayed gait impairments and balance problems that share many features commonly observed in people with PD. We concluded that the MPTP–treated NHP is an appropriate preclinical model for the development and preliminary validation of therapies to alleviate gait impairments and remedy balance problems due to PD.

Requirements to develop a neuroprosthesis that alleviates locomotor deficits due to PD

We aimed to develop a neuroprosthesis based on EES to alleviate locomotor deficits due to PD.EES targets the individual dorsal root entry zones to modulate the motor neurons contained in the spinal segment innervated by the targeted rootlets[22-24].

We sought to leverage this physiological principle to restore the natural spatiotemporal activation of leg motor neurons that is disrupted during walking in people with PD. Therefore, we first determined the natural activation of leg motor neurons in healthy NHPs, and how the MPTP treatment disrupts this activation.

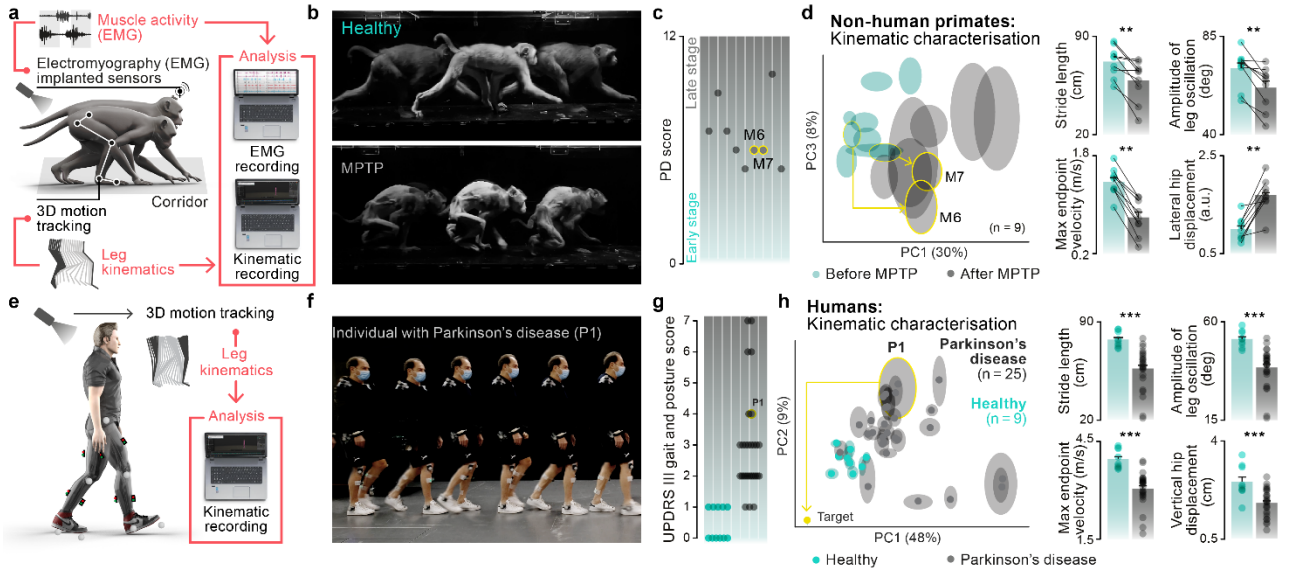

Figure 1 | Locomotor deficits in MPTP-treated NHPs and people with PD. a, Recording platform for NHPs. **b,** Chronophotographs illustrating locomotor deficits in MPTP-treated NHPs. **c,** Distribution of PD scores for 9 MPTP-treated NHPs. **d**, A PC analysis was applied on 83 parameters calculated for each gait cycle. Balloons show mean ±SD of all gait cycles projected in the space spanned by two of the three leading PCs. Bar plots report the mean values for 4 gait parameters highly correlated with PC1. **e,** Recording platform for people with PD. **f,** Chronophotographs illustrating locomotor deficits in a person with PD. **g,** UPDRS scores (gait) of 9 healthy people and 25 people with PD. **h,** Same analysis as in **d** for people, including for P1 and its target gait (yellow), as explain in the section on the clinical trial in the human participant. **,*** $p < 0.01$ and $p < 0.001$, respectively, using Wilcoxon signed rank or rank sum tests. Error bars, sem.

To record muscle activity, we developed a head-mounted system that enabled wireless recordings of electromyography (EMG) from implanted leg muscles while NHPs walked without constraints or tethered electronics. We then visualized motor neuron activity by projecting the recorded EMG signals onto the known anatomical location of the motor neurons that produce these signals (**Fig. 2a**)[22,23,30].

The reconstructed spatiotemporal maps of leg motor neuron activation revealed that walking involves the sequential activation of six well–defined hotspots located in specific regions of the left and right hemicords. The sequential activation of these hotspots reflected the biomechanics of walking[30], successively ensuring weight acceptance, propulsion and leg lift (**Fig. 2a** and **Extended Data Fig. 2a**).

Comparison of maps recorded before and after MPTP treatment revealed that locomotor deficits resulted from diverse alterations in the timing, duration and amplitude of leg motor neuron activity associated with each hotspot (**Fig. 2a** and **Extended Data Fig. 2b**). We thus reasoned that the ensemble of dorsal root entry zones projecting to these 6 hotspots must be targeted to alleviate gait impairments and balance problems.

Tailored implants target the relevant pools of leg motor neurons

We aimed to develop implants with electrode configurations that are optimized to target the dorsal root entry zones projecting to the spinal segments wherein each hotspot is located.

To guide this development, we first studied the anatomy of the Rhesus monkey spinal cord to identify the optimal spatial distribution of electrodes to target these dorsal root entry zones (**Fig.**

2b). The identified electrode distribution informed the design of two 8-electrode arrays that we fabricated using AirRay[31] and electronic dura mater technologies[32,33] (**Extended Data Fig. 3b**).

These electrode arrays were positioned over the epidural surface of the spinal cord in 4 NHPs. The arrays were first advanced to the planned anatomical locations, covering the upper or lower region of the lumbosacral spinal cord. We then delivered single–pulses of EES to elicit muscle responses and leg movements, and monitored these responses to fine-tune the final placement of the arrays. Post-mortem anatomical evaluations confirmed the appropriate and stable location of the electrode arrays over the targeted dorsal root entry zones.

To deliver EES, we interfaced the electrode arrays with the Activa RC implantable pulse generator that we upgraded with wireless communication modules[23]. Recordings of muscle responses when delivering single–pulses of EES confirmed that the electrodes selectively recruited the dorsal root entry zones associated with each of the six targeted hotspots (**Fig. 2c** and **Extended Data Fig. 2c**).

We concluded that the newly-designed electrode arrays possessed the necessary specificity to access the ensembles of hotspots and associated pools of leg motor neurons responsible for locomotor deficits associated with PD.

Motor cortex activity enables decoding of relevant events in NHPs

We then aimed to target the individual dorsal root entry zones of the lumbosacral spinal cord with the appropriate timing to reproduce the natural activation of leg motor neurons during walking. This neuroprosthesis was thus contingent on real-time identification of motor intentions to synchronize EES protocols with the ongoing movements. Concretely, the timing and location of targeted EES bursts must coincide with the activation of the hotspots that produce the ongoing movements.

Motor intentions can be detected using various technologies, including manually-pressed clickers[25], inertial measurement units (IMUs) attached to the limbs[24], and even primary motor cortex activity[23,33-38]. Compared to alternative technologies, detection of motor intentions from motor cortex activity is the only viable strategy in freely-moving NHPs[23,28,36]. However, various studies reported that PD may alter motor cortex activity[10,39-44], suggesting that decoding motor intentions from this region may be compromised. We thus asked whether the timing appropriate to synchronize EES protocols with the activity of the relevant hotspots based on the ongoing movement can be decoded from primary motor cortex activity in our NHP model of PD.

To record neural activity, we inserted microelectrode arrays into the leg region of the primary motor cortex in two MPTP-treated NHPs (M6-M7). We interfaced the microelectrode arrays with a wireless data transmission module[28] that enabled broadband recording of neural activity. We synchronized the acquired neural activity with muscle activity and kinematic recordings[23,36]. Despite pronounced locomotor deficits, both NHPs displayed neuronal firing patterns that were highly regular and phase-locked to the gait cycles (**Fig. 2d**).

We reasoned that these neuronal firing patterns must permit real-time detection of events linked to the activation of the various hotspots. Because alterations of muscle activity occurred during weight acceptance, propulsion and leg lift, the three hotspots associated with these gait phases had to be targeted with EES in each hemicord. Consequently, we devised a strategy to decode the timing of events that coincided with the activation of these 6 hotspots (**Extended Data Fig. 5a**).

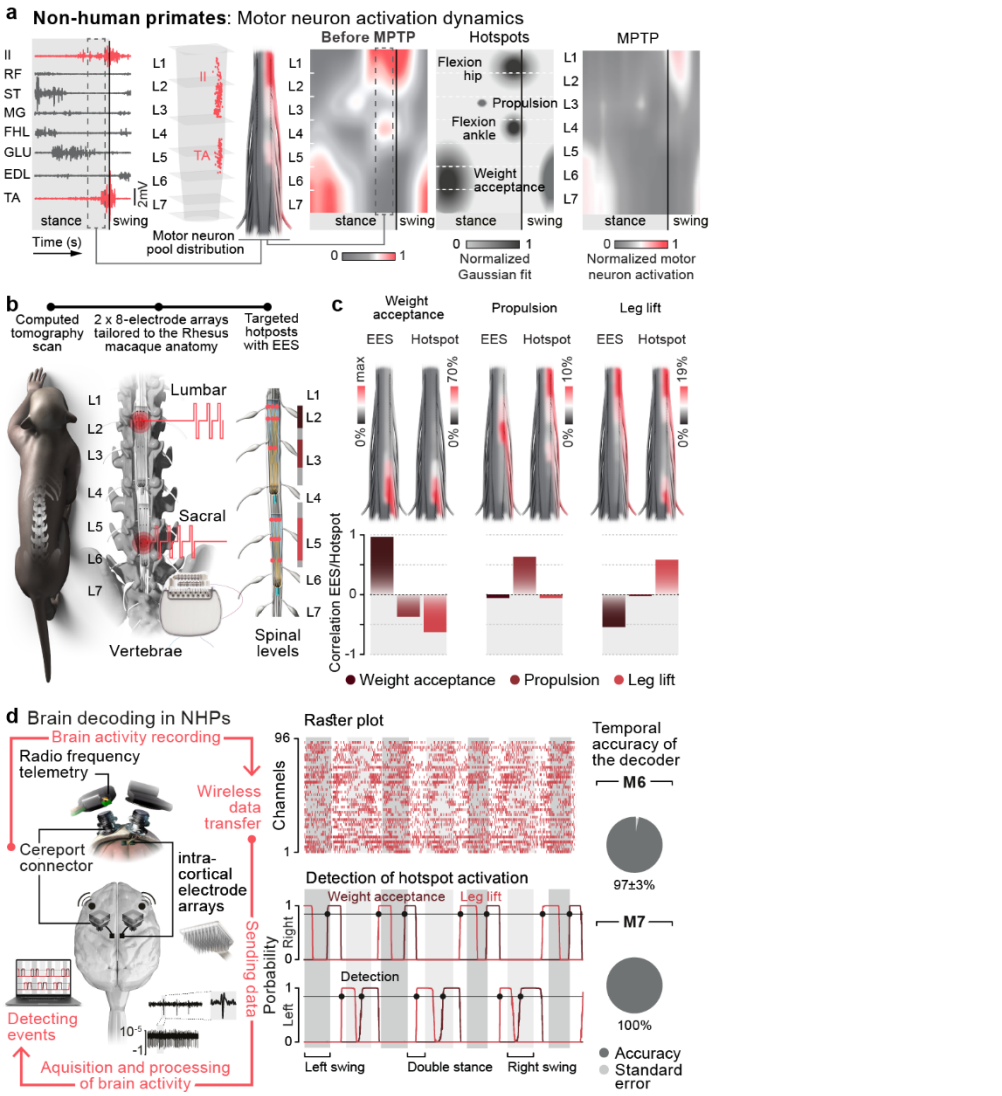

Figure 2 | Design of the spinal cord neuroprosthesis in NHP. a, From left to right: EMG recordings from leg muscles during one gait cycle: iliopsoas (IPS), rectus femoris (RF), semitendinosus (ST), gastrocnemius medialis (MG), flexor hallucis longus (FHL), gluteus (GLU), extensor digitorum longus (EDL) and tibialis anterior (TA); location of IL and TA motor pools along the lumbosacral spinal cord (L1-L7)[14]; projection of EMG signals onto these locations to elaborate a spatial map of motor neuron activation during the highlighted period of the stance phase; average spatiotemporal map of motor neuron activation throughout the entire duration of the gait cycle (n = 20 gait cycles); 3 hotspots of the right hemicord extracted by fitting a Gaussian model: weight acceptance, propulsion and leg lift that comprises anatomically separated ankle and hip flexion motor neuron activations; and changes in the map after MPTP (n = 17 gait cycles). **b,** CT scan of the spine determining the design of two 8-electrode arrays that target the 3 hotspots from each side, highlighted by specific colors in the vertical bars near the spinal cord. **c,** Spatial maps of activation evoked by EES (left) and of the targeted hotspot (right). Bars plots report the correlations between the maps evoked by EES and the 3 targeted hotspots. **d,** Wireless modules are screwed onto skull-mounted pedestals to transmit wideband neural activity recorded using microelectrode arrays inserted into the leg region of left and right motor cortex. Raster plots of neural activity and concomitant probability of activation of weight acceptance and leg lift hotspots over three successive gait cycles calculated by the rLDA algorithm (M6 after MPTP administration). Dots indicate moments when the probability crosses the detection threshold. The pie charts show the mean ± sem accuracy of the detections for M6 (178 events) and M7 (256 events) calculated by offline analysis using cross-validation.

To validate this strategy, we performed longitudinal recordings in M6 and M7 once they had reached stable gait impairments after MPTP treatment. We configured a regularized linear discriminant analysis (rLDA) algorithm that accurately detected the activation of these hotspots using motor cortex activity[23,33,35,36,45]. The rLDA algorithm maintained accurate detection of the events associated with each hotspot across four sessions spanning a period of several weeks (**Fig. 2d**).

We concluded that motor intentions can be reliably decoded from motor cortex activity during walking in our NHP model of PD, and that these predictions are suitable to synchronize the timing and location of EES bursts to alleviate locomotor deficits.

The brain-controlled neuroprosthesis reduces locomotor deficits in NHPs

We then aimed to interface motor cortex activity with the timing and location of EES bursts to conceive a wireless brain-controlled neuroprosthesis operating in closed-loop, and asked whether this neuroprosthesis was effective to alleviate gait impairments and balance problems observed in MPTP-treated NHPs.

Three NHPs (M8, M9 and M11) had developed substantial gait impairments and balance problems following the MPTP-treatment. In a single neurosurgical intervention, we inserted two microelectrode arrays in the left and right motor cortex, two electrode arrays over the spinal cord, an implantable pulse generator in the abdomen, and EMG electrodes into selected leg muscles (**Fig. 3a**, **Extended Data Fig. 3a)**. We configured a control computer that acquired the neural signals, detected events from cortical activity, and sent updated sequences of EES bursts to the implantable pulse generator in order to translate motor intentions into the activation of leg motor neurons to facilitate walking. This ensemble of neurotechnologies established a digital bridge between the brain and spinal cord that operated wirelessly and in real-time.

We noticed that the delivery of EES led to responses in the motor cortex. To mitigate the impact of these responses on detection of gait events, we calibrated the decoders using two minutes of neural activity without and with EES[23] (**Extended Data Figure 5b**). This approach enabled accurate detection of movement intentions even in the presence of EES (**Fig. 3b** and **Extended Data Figure 7a-b**).

This brain-controlled neuroprosthesis immediately alleviated gait impairments and balance problems in the 3 tested MPTP-treated NHPs (**Extended Data Fig. 7b, Supplementary Video 2**). The NHPs completed the locomotor tasks as rapidly as before the MPTP treatment (**Fig. 3b**). As intended, the neuroprosthesis restored the natural spatiotemporal activation of leg motor neurons during walking (**Fig. 3c**), which translated into improvements of gait quality (**Fig. 3d**, **Extended Data Fig. 7b**) and balance (**Extended Data Fig. 7b**).

The neuroprosthesis also improved posture. To quantify these improvements, we transformed computerized tomography scans into a tridimensional biomechanical model of NHPs onto which we morphed whole-body kinematics. This morphing procedure revealed a decrease in spine curvature during walking with the neuroprosthesis (**Extended Data Fig. 7d**).

The neuroprosthesis additionally improved gait and balance during skilled locomotion. The NHPs M8 and M11 progressed very slowly when negotiating the rungs of a horizontal ladder. M11 often fell during the ladder crossings. The neuroprosthesis immediately restored a natural progression along the ladder and reduced falls to nearly zero (**Extended Data Fig. 7e** and **Supplementary Video 2**).

These results were reproduced over successive days, during which we implemented the same decoder and EES protocols without recalibration (**Fig. 3d**, **Extended Data Fig. 7b,c,e**).

The location (**Extended Data Fig. 2c**) and timing of EES (**Extended Data Fig. 8**) were critical to mediate improvement, since changing any of these parameters reduced locomotor performance.

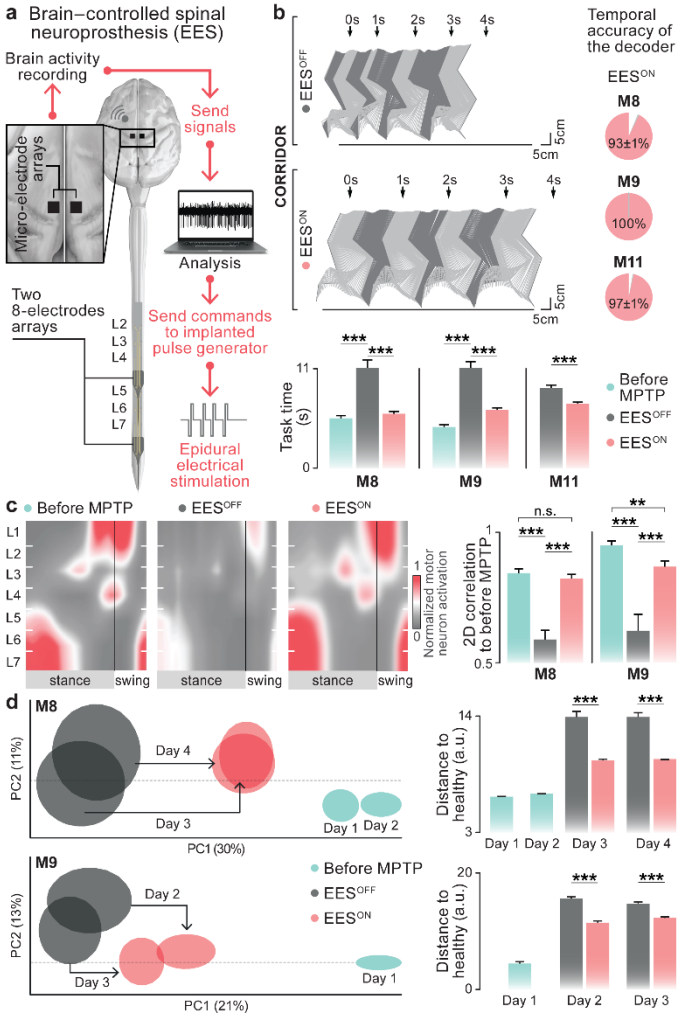

Figure 3 | The neuroprosthesis alleviates gait impairments and balance problems in MPTP-treated NHPs. a, Scheme of the brain-controlled neuroprosthesis. **b,** Stick diagram decomposition of leg kinematics during 4s of locomotion (animal M9) after MPTP administration without (EES^{OFF}) and with (EES^{ON}) the neuroprosthesis. Pie charts report the accuracy of the decoder (n = 516, 618 and 612 events for M8, M9 and M11, respectively) during walking. Bar plots report the average task time when crossing a 3m-long straight corridor (n = 16, 21, 8 trials for M8, 11, 12, 7 trials for M9, and 15, 22 trials for M11 across conditions from left to right). **c,** Spatiotemporal maps of motor neuron activation for M8. Bar plots report the surface correlation between motor neuron activation maps for the various conditions (n = 17, 39 and 33 steps for M8, and 11, 26 and 34 steps for M9 across conditions from left to right). The maps were normalized to 1 using the 95th percentile of the envelope over the entire session (EES^{OFF} and EES^{ON} datasets were recorded in the same session, Before MPTP dataset was recorded in a separate session). **d,** PC analysis of gait kinematics, as in Fig. 1. The balloons show mean ± SD of all gait cycles of one of the experimental conditions. Bar plots report the Euclidean distance in the full 83-dimensional space between each gait cycle and the mean values across all the gait cycles recorded before MPTP administration (n = 26, 51, 27, 81, 50, 45 gait cycles for M8, 63, 62, 45, 140 and 55 gait cycles for M9 across conditions from left to right). Gait patterns from M8 were recorded in two days before the MPTP treatment (days 1 and 2) and two days after the treatment (days 3 and 4). For M9, gait patterns were recorded in one day before the MPTP treatment (day 1) and two days after the treatment (days 2 and 3). *, **, *** significant difference at $p < 0.05$, $p < 0.01$, $p < 0.001$, respectively, using Wilcoxon rank sum test or the Monte Carlo permutation test. Error bars, sem.

The neuroprosthesis complements DBS in MPTP-treated NHPs

DBS is the primary neurosurgical intervention to alleviate motor signs of PD, but benefits on locomotion have been variable, if not detrimental[4-8]. We thus asked whether our neuroprosthesis can complement DBS to address the entire range of motor signs associated with PD.

To address this question, we implanted DBS electrodes into the left and right subthalamic nuclei in addition to the brain-controlled neuroprosthesis in M9. Structural magnetic resonance imaging confirmed the accurate location of DBS electrodes (**Fig. 4a**). DBS delivered at the known therapeutic frequency of 125 Hz (but not 20 Hz) improved general mobility and alertness, which translated into a higher number of completed trials and faster walking speeds (**Extended Data Fig. 9a-c**). However, PC analysis applied to kinematic quantifications revealed that the legs remained exaggeratedly flexed during the stance phase, indicating a lack of extension and propulsion that restricted the length and height of steps (**Extended Data Fig. 9d**).

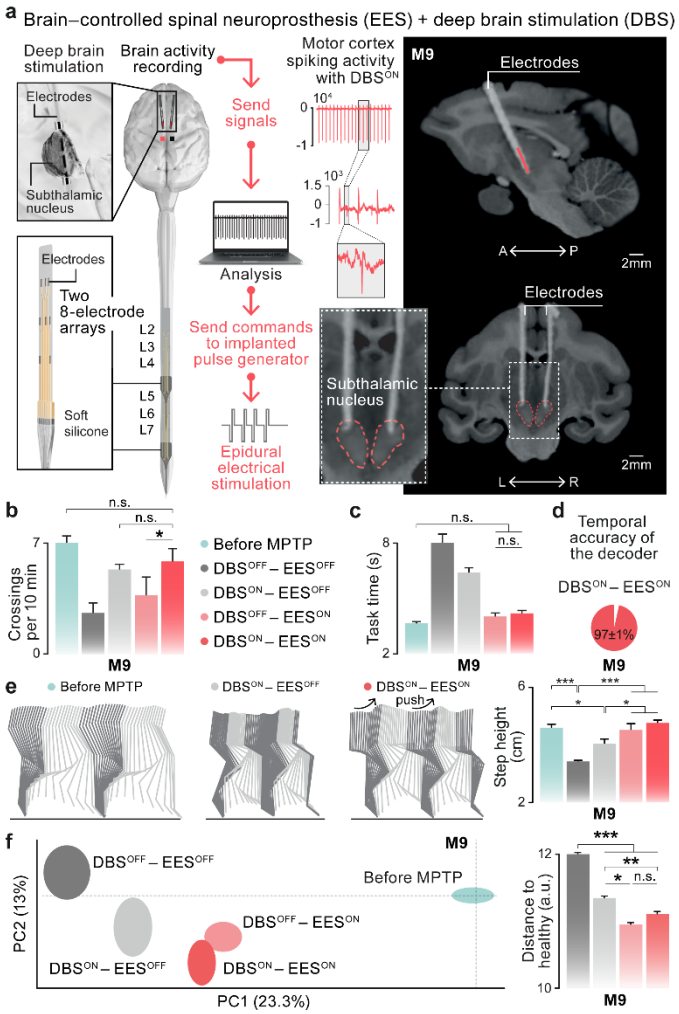

Figure 4 | The neuroprosthesis complements DBS of the subthalamic nucleus to alleviate locomotor deficits in MPTP-treated NHPs. a, Scheme illustrating the insertion of DBS electrodes in the STN of M9, and anatomical location of DBS implants as shown on post-mortem MRI. **b,** Bar plots reporting the number of corridor crossings within 10 minutes (number of trials, before MPTP: 24; after MPTP: 19; DBS: 17; BSI: 19; BSI + DBS: 22). **c,** The bar plots report the task time (number of gait cycles, before MPTP: 11; after MPTP: DBS^{OFF} - EES^{OFF}: 7; DBS^{ON} - EES^{OFF}: 5; DBS^{OFF} - EES^{ON}: 9; DBS^{ON} - EES^{ON}: 7). **d,** Pie chart reports the accuracy of the decoder during DBS^{ON} - EES^{ON} trials (n = 145 events) measured

during the online use of the neuroprosthesis. **e,** Stick decomposition illustrating the changes in leg kinematics in M9 induced by EES when combined with DBS after the MPTP treatment, as compared to DBS alone and to before the MPTP treatment. Barplots indicate the average step height across conditions. **f,** PC analysis of gait kinematics, as in Fig 3, under the various combinations of EES and DBS on or off (number of gait cycles, before MPTP: 39; after MPTP: DBS^{OFF} - EES^{OFF}: 47; DBS^{ON} - EES^{OFF}: 37; DBS^{OFF} - EES^{ON}: 60; DBS^{ON} - EES^{ON}: 43). The balloons show mean ± SD of all gait cycles of one of the experimental conditions. The bar plot reports the Euclidean distance in the full 83-dimensional space between each gait cycle and the mean values across all the gait cycles recorded before MPTP administration. *, **, *** significant difference at $p < 0.05$, $p < 0.01$, $p < 0.001$, respectively, using Wilcoxon rank sum test or the Monte Carlo permutation test. Error bars, sem.

When the neuroprosthesis and DBS were turned on concomitantly, M9 not only showed increased alertness (**Fig. 4b**) but also exhibited immediate improvement of gait kinematics that led to step elevations (**Fig. 4e**) and walking speeds closer to those quantified before the MPTP treatment (**Fig. 4c**). Adding the neuroprosthesis to the DBS substantially improved gait quality (**Fig. 4f**). Yet, these improvements did not go beyond those already achieved by using the neuroprosthesis alone (**Fig. 3** and **Extended Data Fig. 7**). Decoding of events to synchronize EES bursts to ongoing movements remained accurate during the use of DBS (**Fig. 4d**).

Together, these experiments in our NHP model of PD suggested that biomimetic modulation of the neuronal circuits located in the lumbosacral spinal cord complements DBS of the subthalamic nucleus to alleviate gait impairments and balance problems due to the loss of dopamine-producing cells in NHPs. These observations compelled us to test this treatment in people with PD.

Motor cortex activity enables decoding of gait events in people with PD

We previously established a digital bridge between the brain and spinal cord that enabled brain-controlled modulation of EES protocols to regain natural walking in a person with paralysis due to spinal cord injury[34]. While this previous work showed the technological feasibility of implementing a brain-controlled neuroprosthesis in people with PD, the possibility of decoding motor intentions from cortical activity in people with PD remained unknown. Indeed, PD involves a widespread, slow-evolving alteration of neural networks that may not be entirely reproduced using MPTP treatments delivered over restricted time windows in NHPs. Therefore, we sought to verify the conceptual feasibility of detecting events from motor cortex activity in people with PD to synchronize EES with the ongoing movements.

Under the framework of a physician-sponsored clinical study (IDE protocol G180097), two participants with idiopathic PD and motor fluctuations received bilateral subdural electrode arrays over the primary motor cortex[46]. The arrays were interfaced to the Summit RC+S implanted pulse generators, which enabled wireless streaming of electrocorticogram (ECoG) signals to an external computer.

We implemented the same event-detection strategy as used previously in NHPs[23,33,36] and people[35,38] to detect events associated with the activation of hotspots from ECoG signals (**Fig. 5** and **Extended Data Fig. 6a**). In both participants P2 and P3, the algorithm detected the events linked to leg lift with high accuracy (**Fig. 5** and **Extended Data Fig. 6b**).

These results demonstrated the conceptual feasibility of decoding events from primary motor cortex activity to synchronize EES to the ongoing movements in people with PD.

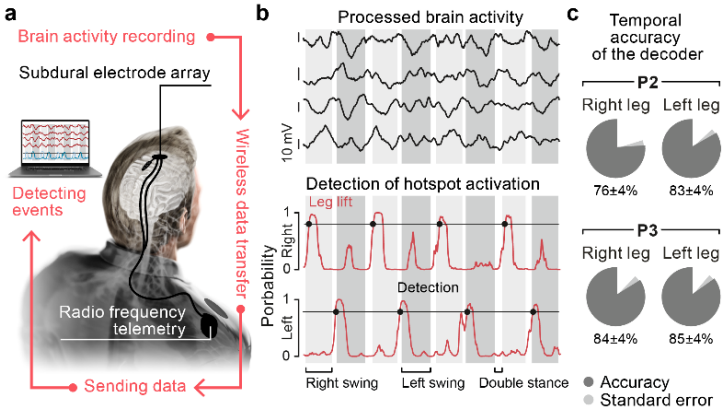

Figure 5 | Accurate decoding of gait events from motor cortex activity in people with PD. a, Quadripolar cortical paddle inserted subdurally over the motor cortex, and connected to the Medtronic Summit RC+S device to acquire epicortical signals wirelessly. The neural signals and probability of leg lifts are shown while P2 walks freely along a corridor. The pie charts show the mean ± sem accuracy of the detections for P2 (events: left: 64; right: 62) and P3 (events: left: 70; right: 74) calculated by offline analysis using cross-validation.

Development of a neuroprosthesis to alleviate locomotor deficits in humans

Finally, we enrolled a 62 years old male (P1) who presented with a 30-year history of PD in the first-in-human STIMO-PARK clinical trial (clinicaltrial.gov ID: NCT04956770, **Supplementary Information**). While DBS and finely-tuned dopaminergic replacement therapies improved cardinal signs of PD, he had developed severe locomotor deficits that led to 2 to 3 falls per day. P1 exhibited the common locomotor deficits observed in our cohort of people with PD (**Fig. 1h** and **Fig. 6a**), including marked gait asymmetry, reduced stride length, balance problems as well as episodes of freezing-of-gait and frequent falls. We thus asked whether the neuroprosthesis could complement DBS and dopaminergic replacement therapies to alleviate his persistent locomotor deficits.

The neuroprosthesis aims to reestablish the natural activation of leg motor neurons during walking. Contrary to NHPs that acted as their own control, we could not record the natural spatiotemporal activation of leg motor neurons underlying walking prior to the onset of PD in P1. To remedy this limitation, we generated a personalized neurobiomechanical model[47] actuated by a reflex-based circuit that allowed us to estimate the optimal kinematics and muscle activity patterns during walking that was expected by P1 in the absence of PD (**Fig 6a**). As in NHPs, the occurrence of weight acceptance, propulsion and leg lift coincided with the activation of 6 hotspots that emerged in specific regions of the spinal cord (**Fig. 6b**). Compared to simulations, we detected changes in the timing, location and amplitude of these 6 hotspots (**Fig. 6b)**. We concluded that the ensemble of dorsal root entry zones projecting to the 6 hotspots had to be targeted with EES.

To target these dorsal root entry zones, we repurposed a clinically-approved electrode array commonly used to treat neurogenic pain[24]. The neurosurgical implantation of this array was guided by a personalized anatomical model of the spine that we generated using high-resolution computerized tomography and magnetic resonance imaging[25] (**Fig. 6c)**. This model determined the optimal location of the electrode array to recruit the targeted dorsal root entry zones. The neurosurgical intervention was performed under full anesthesia. Once the electrode array was advanced to the planned location, we delivered single pulses of EES to elicit responses in leg muscles. These electrophysiological recordings confirmed that the electrode array was able to recruit all 6 targeted hotspots specifically (**Fig. 6d** and **Extended Data Fig. 4a**). We finally interfaced the

electrode array with the Activa RC implantable pulse generator, which we upgraded with wireless communication modules[25], as in NHPs[23].

The neuroprosthesis alleviates locomotor deficits in a person with PD

Unlike NHPs, people tolerate wearable sensors attached to their limbs[48]. Signals from wearable sensors are suitable to synchronize EES protocols to ongoing movements to restore walking in people with spinal cord injury[24,25]. Before considering the surgical implantation of a system to record cortical activity[34], we asked whether this noninvasive approach was sufficient to control the neuroprosthesis in P1.

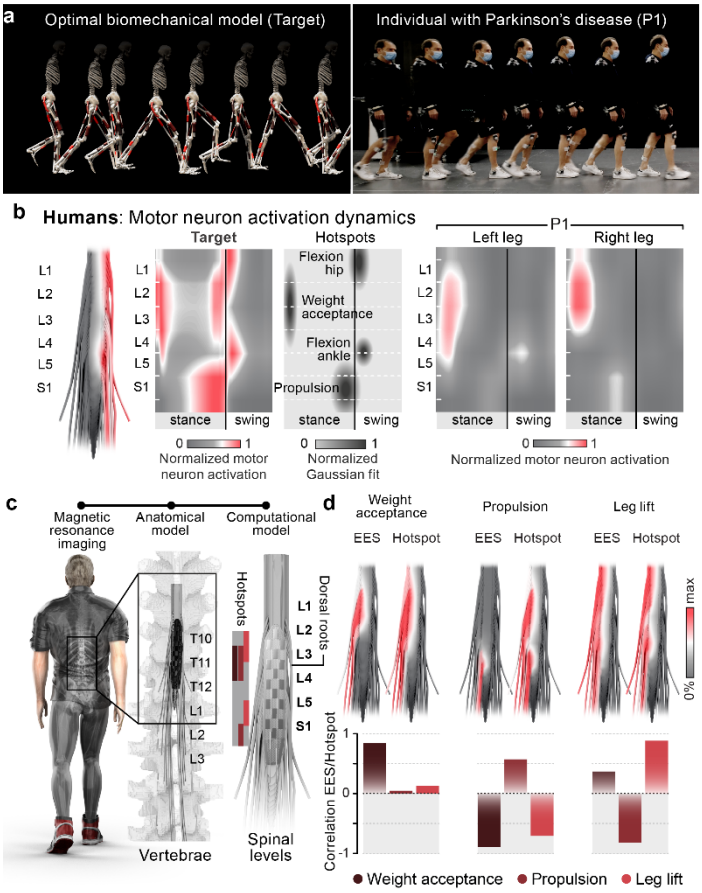

Figure 6 | Design of the neuroprosthesis for people with PD. a, Chronophotographs illustrating an optimal gait for P1 based on a personalized OpenSim neurobiomechanical model (target gait), and gait deficits of P1, also reported in Fig 1. **b,** Same analysis as in **Fig. 2a** here for P1, including their target spatiotemporal activation of leg motor neurons. **c,** The illustration shows the anatomical model of P1's spine reconstructed from MRI and CT. This model was used to determine the surgical placement of a 16-electrode array as shown on the illustration on the right. The color-coded matrix shows the caudo-rostral locations of the three hotspots for each hemicord. **d,** Same analysis as in **Fig. 2c** here for P1.

We developed a new clinical-grade software running on a tablet that acquired signals from wearable inertial measurement units (IMUs) attached to the left and right legs, detected events associated with the onset of the relevant hotspots based on the same rLDA algorithm as in NHPs and people with PD, and sent updated sequences of EES protocols to the implanted pulse generator (**Fig. 7a** and **Extended Data Fig. 3a**). This chain of hardware and software translated the detection

of motor intentions from IMUs into the modulation of EES protocols to facilitate the intended leg movements (**Fig. 7b-c)**. The software is operated through touch-screen interfaces that enable rapid configuration of the algorithm and EES protocols.

We first quantified the therapeutic impact of this neuroprosthesis in the presence of the best therapeutic strategy for P1, which involved dopamine replacement therapy and DBS. The neuroprosthesis immediately restored the natural spatiotemporal activation of leg motor neurons during walking (**Fig. 7d**), which translated into pronounced improvements of gait and balance (**Fig. 7c,e, Extended Data Fig. 10d** and **Supplementary Videos 2 and 3**). Concretely, the neuroprosthesis restored gait symmetry by reinforcing the activity of muscles from the most affected leg (**Extended Data Fig. 10d**). In addition, EES bursts augmented the activation of propulsion hotspots, which produced longer and higher foot trajectories (**Extended Data Fig. 10d**). Lastly, EES bursts targeting weight acceptance hotspots reinforced stability during stance (**Extended Data Fig. 10d**), which improved balance.

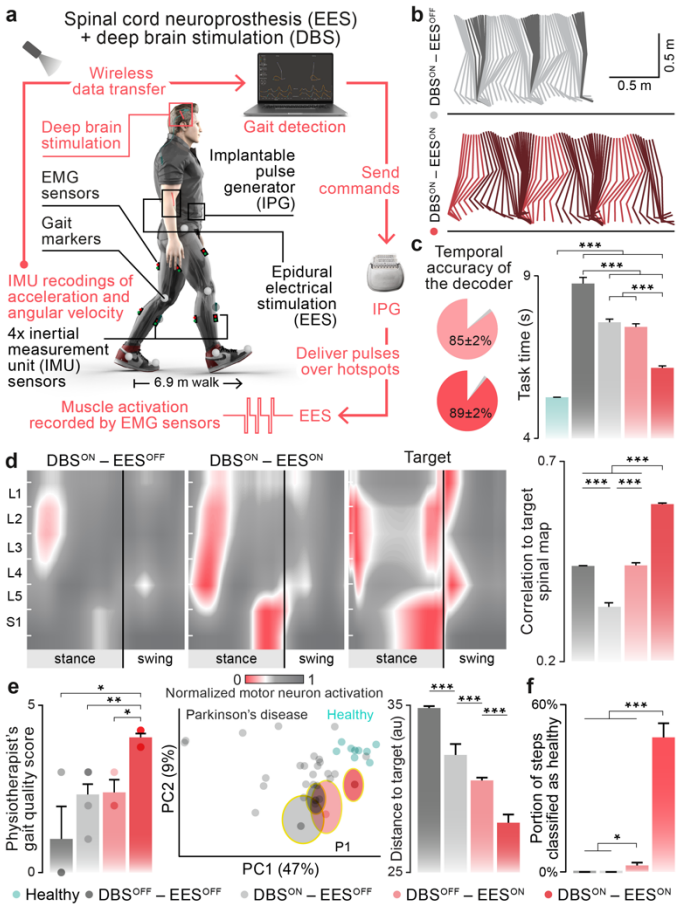

Figure 7 | The neuroprosthesis alleviates gait impairments in a person with PD. a, Scheme illustrating the neuroprosthesis combined with DBS of the subthalamic nucleus in participant P1. **b,** Stick diagram decomposition of leg kinematics during 3s of locomotion with DBS^{ON} - EES^{OFF} and DBS^{ON} - EES^{ON}. **c,** Pie charts report the accuracy of the decoder during DBS^{OFF} - EES^{ON} (n =462 events) and DBS^{ON} - EES^{ON} (n = 328 events) while P1 walks overground measured during the online use of the neuroprosthesis. Bar plot reports task time (number of trials: DBS^{OFF} - EES^{OFF}: 25; DBS^{ON} - EES^{OFF}: 24; DBS^{OFF} - EES^{ON}: 38; DBS^{ON} - EES^{ON}: 32). **d,** Spatiotemporal maps of motor neuron activation and bar plots reporting the surface correlation between motor neuron activation maps during DBS^{ON} - EES^{OFF} (n = 66 gait cycles) and DBS^{ON} - EES^{ON} (n = 91 gait cycles) compared to the map from the target gait (n = 168 gait cycles). Sem, calculated using bootstrapping. **e,** Bar plots report gait quality score evaluated by physiotherapists (number of trials:

DBS^{OFF} - EES^{OFF}: 2; DBS^{ON} - EES^{OFF}: 2; DBS^{OFF} - EES^{ON}: 5; DBS^{ON} - EES^{ON}: 5). The scatter plot shows the PC analysis of gait kinematics applied on 39 parameters. The balloons show mean ± SD of all gait cycles of P1 in one of the experimental conditions (number of gait cycles: DBS^{OFF} - EES^{OFF}: 255; DBS^{ON} - EES^{OFF}: 105; DBS^{OFF} - EES^{ON}: 317; DBS^{ON} - EES^{ON}: 172) projected in the space spanned by PC analysis of kinematics of 9 healthy people and 25 people with PD shown in Fig. 1h. Each dot shows the mean of all gait cycles of one of the 9 healthy people (grey) and 25 people with PD (green). Bar plots report the mean Euclidean distance in the full 39-dimensional space between each gait cycle in a given condition and the mean gait cycle of the target gait. **f,** Bar plots report the portion of steps classified as healthy using a linear discriminant analysis decoder calibrated on all the steps from 25 people with PD and 9 healthy age-matched people (data reported in **e**). *, **, *** significant difference at $p < 0.05$, $p < 0.01$, $p < 0.001$, respectively, using Wilcoxon rank sum test or the Monte Carlo permutation test. Error bars, sem.

To assess whether gait patterns from P1 were more similar to those of people with PD or to healthy people, we implemented a classification using a LDA decoder[26]. We calibrated this decoder on gait parameters calculated from kinematic recordings of 25 people with PD and 9 healthy age-matched controls. We then used the decoder to classify whether each gait pattern performed by P1 was more similar to gait patterns from people with PD or healthy people. When the neuroprosthesis was turned on, the majority of steps performed by P1 were classified as gait patterns from healthy people (**Fig. 7f**).

Improvements were also observed when the DBS was turned off, albeit to a lesser extent (**Fig. 7** and **Extended Data Fig. 10**). Neurological assessments measured by Unified PD Rating Scores (UPDRS)[49] highlighted the complementary between the neuroprosthesis and DBS to alleviate locomotor deficits in P1 (MDS UPDRS III score: DBS^{OFF} - EES^{OFF}: 65; DBS^{ON} - EES^{OFF}: 29; DBS^{ON} - EES^{ON}: 24; see gait subscores in **Supplementary Table 10**), as further confirmed by subjective assessments conducted by physical therapists (**Fig. 7e**) and by P1 (**Extended Data Fig. 10d**) using gait quality scores. As in NHPs, the neuroprosthesis maintained high accuracy in the decoding of events associated with the activation of the hotspots, both with or without the use of DBS (**Fig. 4c**, **Extended Data Fig. 10e**).

The neuroprosthesis reduces freezing-of-gait

Freezing-of-gait refers to the episodically hampered ability to move the legs. Freezing-of-gait is one of the most debilitating locomotor deficits of PD, for which current treatment strategies are poorly effective[4,50 2,37].

Despite DBS and finely-tuned dopaminergic replacement therapies, P1 exhibited frequent freezing-of-gait episodes that occurred when turning and when passing through narrow paths. These episodes led to multiple falls per day, which severely affected his quality of life.

While MPTP-treated NHPs and people with PD show comparable gait impairments and balance problems, this preclinical model of PD rarely leads to freezing-of-gait[51]. Therefore, we had not been able to evaluate the benefits of our neuroprosthesis on this locomotor deficit in NHP models.

To be able to quantify the impact of the neuroprosthesis on freezing-of-gait in P1, we designed a path that involved frequent turns, crossing of obstacles, and passing through narrow spaces (**Fig. 8a**). P1 experienced frequent freezing-of-gait episodes when navigating this environment. When the neuroprosthesis was turned on, freezing-of-gait nearly vanished, both with and without DBS (**Fig. 8a**). The closed-loop operations of the neuroprosthesis remained highly accurate despite the navigation through the complex environment of this task.

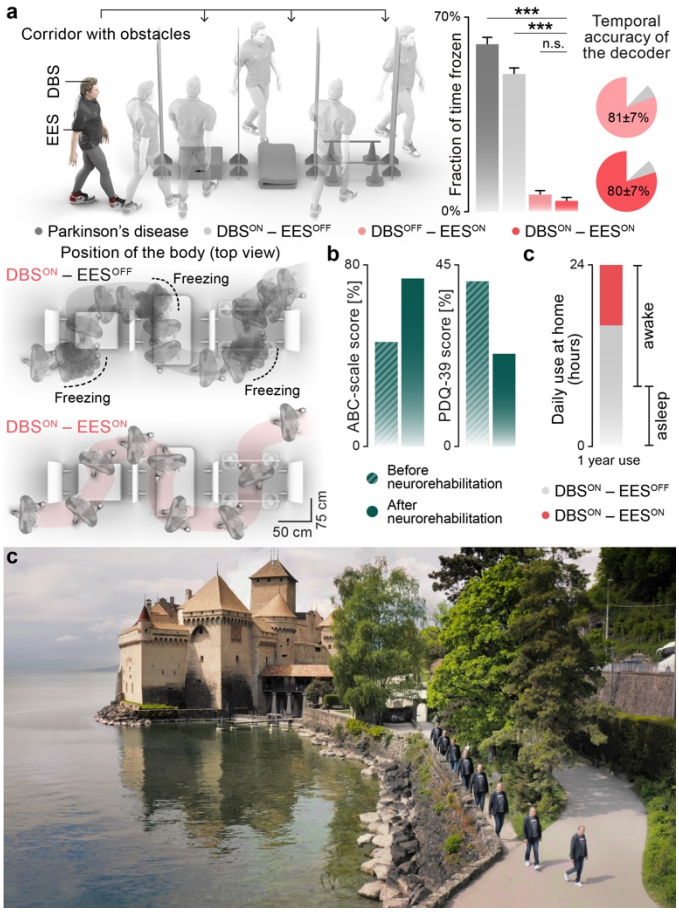

Figure 8 | The neuroprosthesis reduces the frequency of freezing of gait, improves balance, increases quality of life and supports mobility in community settings. a, Scheme illustrating a circuit that comprises three narrow passages with obstacles that provoked freezing of gait in P1. Below is shown the successive position of the body while P1 navigates along this circuit with DBS^{ON} - EES^{OFF} and DBS^{ON} - EES^{ON}. Broken lines denote the occurrence of freezing of gait events. The bar plots report the fraction of time during which P1 experienced freezing (measurement duration: DBS^{OFF} - EES^{OFF}: 39.0s; DBS^{ON} - EES^{OFF}: 51.3s; DBS^{OFF} - EES^{ON}: 27.7s; DBS^{ON} - EES^{ON}: 23.3s). The pie charts report the accuracy of the decoder during DBS^{OFF} - EES^{ON} (n = 26 events) and DBS^{ON} - EES^{ON} (n = 29 events) while navigating the circuit measured during the online use of the neuroprosthesis. **b,** Bar plots reporting gains in balance measured using ABC scale questionnaire, and the quality of life measured using the PDQ-39 questionnaire after neurorehabilitation supported by the neuroprosthesis. **c,** Pie chart shows the daily independent use of the neuroprosthesis at home reported by P1 at his follow-up one year after the implantation. The chronophotograpy shows P1 using the neuroprosthesis for recreational walks in the nature. *** significant difference at $p < 0.001$ using Monte Carlo permutation test. Error bars, sem.

Rehabilitation supported by the neuroprosthesis reduces locomotor deficits

Many studies suggested that gait rehabilitation reduces locomotor deficits in people with PD, and that the additional support of neuromodulation therapies may further augment the impact of rehabilitation. We thus sought to test this possibility in P1.

P1 followed a rehabilitation program augmented by the neuroprosthesis that involved a variety of exercises, including walking on basic and complex terrains, navigating outdoors in community settings, balance training, and basic physical therapy. Rehabilitation sessions were conducted 2 to 3 times per week, for a duration of 3 months.

Quantifications of locomotor deficits using well-established clinical scores and tests revealed substantial improvements in endurance and balance (**Fig. 8b**), combined with a reduction of freezing

of gait. Frequent use of the neuroprosthesis during gait rehabilitation translated into a pronounced increase in quality of life (**Fig. 8** and **Extended Data Fig. 10h-i**).

The neuroprosthesis supports mobility in community settings

P1 was eager to integrate the neuroprosthesis in his daily life to support his activities of daily living. To enable the transition to independent use in community settings, we designed a user-friendly interface that allowed him to configure and operate the neuroprosthesis independently.

P1 has now been utilizing the neuroprosthesis for nearly two years, for about 8 hours per day, only switching the neuroprosthesis off when sitting for long periods of time or while sleeping. The neuroprosthesis enabled P1 to enjoy recreational walks in nature over several kilometers without any additional assistance (**Fig. 8c** and **Supplementary movie 4**).

DISCUSSION

We developed a neuroprosthesis that alleviated gait impairments, balance problems and freezing-of-gait due to PD. Moreover, gait rehabilitation augmented by the neuroprosthesis improved the neurological status of the participant who reported improvement in his quality of life.

While previous therapies focused on the neuronal circuits in the brain that are directly affected by the loss of dopamine-producing cells, our neuroprosthesis targeted the neuronal circuits in the lumbosacral spinal cord that ultimately produce walking, and are *a priori* not directly affected by PD. Central to the development of this neuroprosthesis was the understanding that EES modulates the activity of neuronal circuits involved in the production of locomotion by targeting large-diameter afferent fibers when they enter the spinal cord within the individual dorsal root entry zones. We translated this knowledge into a closed-loop neuroprosthesis that achieved biomimetic modulation of the lumbosacral spinal cord in real-time in order to compensate for the abnormal activation of leg motor neurons due to PD.

We developed this neuroprosthesis in a cohort of MPTP-treated NHPs, but validated this therapeutic concept in only one person with PD. PD leads to a large spectrum of neurological profiles associated with distinct locomotor deficits. Consequently, it remains unclear whether the neuroprosthesis will be effective to alleviate gait impairments, remedy balance problems and reduce freezing of gait across the entire population of people with PD. Future studies will thus have to identify the responders of this therapy.

Scaling up this therapy is contingent on purpose-built technologies that are optimized for the specific requirements of people with PD. First, the personalization of precise EES protocols requires a portfolio of tailored electrode arrays that can target the ensemble of dorsal root entry zones involved in the control of leg motor neurons in each person with PD, combined with a versatile neurostimulation platform for rapid, closed-loop control of EES. Second, the real-time synchronization of the neuroprosthesis with the motor intentions requires the identification of the optimal trade-off between invasiveness, reliability and practicality of the technology used to detect motor intentions. Non-invasive wearable sensors are the preferred solution as long as the detections are reliable and the sensors practical to use in daily life. These signals were sufficient to operate the neuroprosthesis in our participant with high accuracy. Because PD induces a broad range of neurological deficits, it is possible that more severe conditions and/or locomotor deficits may require more precise signals based on invasive technologies. We showed here that motor intentions can be decoded from cortical activity with high-precision using minimally-invasive implants. We previously

leveraged this understanding to design a digital bridge between the brain and spinal cord that restored natural walking in an individual with paralysis due spinal cord injury[34]. The conceptual and technological feasibility of a brain-controlled neuroprosthesis is thus well established. Alternatively, one can take advantage of DBS electrodes to monitor neural activity from the subthalamic nucleus. We showed that normal and pathological gait events can be decoded in real-time from these recordings in people with PD[54]. This methodology is attractive, since many people with PD receive DBS electrodes before experiencing untreatable locomotor deficits that would encourage them to be implanted with our neuroprosthesis.

We are committed to developing purpose-built technologies optimized for the specific requirements of people with PD, to identifying the patients who respond to this therapy, and thus to informing the design of a pivotal trial to demonstrate the safety and efficacy of the neuroprosthesis for alleviating locomotor deficits of people with PD.

FUNDING

Defitech Foundation, Roger de spoelberch Prize, Onward Medical, CAMS Innovation Fund for Medical Sciences (CIFMS) grant 2021-1-I2M-034, National Natural Science Foundation of China Grant 81941012 and 82161138027, PDWALK ERANET JP cofunND 2-NT (ANR, FNS, ZonMw), Parkinson Schweiz foundation, the European Community's Seventh Framework Program (NeuWalk), Consolidator Grant from the European Research Council, the Wyss Center for Bio- and Neuroengineering, Bertarelli Foundation, a Marie Curie Fellowship to D.A.B., Marie Curie COFUND EPFL fellowships to T.M. and G.S., a Morton Cure Paralysis Fund fellowship to T.M., a Whitaker foundation fellowship to M.G.P., and the Swiss National Science Foundation including the National Center of Competence in Research (NCCR) in Robotics, Sino-Swiss Science and Technology Cooperation (IZLCZ3_156331), NanoTera.ch program (SpineRepair) and Sinergia program (CRSII3_160696).

METHODS

Animal husbandry. Experiments were approved by the Institutional Animal Care and Use Committee of Bordeaux (CE50, France) under the license number 50120102-A and performed in accordance with the European Union directive of 22 September 2010 (2010/63/EU) on the protection of animals used for scientific purposes in an AAALAC-accredited facility (Chinese Academy of Medical Sciences, Beijing, China). Eleven male macaque monkeys M1-11 (10 *Macaca mulatta,* 1 *Macaca fascicularis*; **Supplementary Table 1**) aged between 4 and 6 years old, and weighing between 4.1 kg and 7.1 kg (5.88 ± 0.72 kg) were housed individually in cages designed according to European guidelines (2 m × 1.6 m × 1.26 m). Environmental enrichment included toys and soothing music.

Behavioural training of NHPs. The animals were trained to walk on a motorized treadmill, across a straight corridor, and across a horizontal ladder course that consisted of a platform at the beginning and at the end of the course and seven equally spaced rungs in-between. Plexiglas enclosures (treadmill: 110 cm × 40 cm × 70 cm; corridor/ladder: 300 cm × 35 cm × 70 cm) were used to keep the animals within the field of view of the cameras. Food pellets and fruits rewarded appropriate behaviour. Additional food to complete daily dietary requirements was provided after training.

Preparation and assessment of the NHP model of PD. We administered 1-methyl-4-phenyl-1,2,3,6-tetrahydropyridine (MPTP) in M1-11 according to the previously published protocol[55-61]. Animals were treated daily (7:00 A.M.) with MPTP hydrochloride (0.2 mg/kg, i.v.; Sigma, St. Louis, MO) dissolved in saline according to a previously described protocol[8]. This protocol describes a reproducible MPTP cumulative dosing regimen that leads to the first appearance of Parkinsonian clinical signs after 15 ± 1 injections (i.e., a cumulative dose of 3.0 ± 0.2 mg/kg). Neurological deficits were evaluated every morning at 9 am in home cages for 30 min. Two blinded observers who were not involved in the study quantified these deficits using a validated Parkinsonian Disability (PD) score[62] assessing general level of activity, body posture, vocalization, freezing, tremor and frequency/rigidity of arm movements. We stopped the injections when the deficits corresponded to late-stage Parkinsonism, defined by PD score of 5 or higher. Injections were repeated if the monkeys displayed recovery of gait and balance. The kinetics of nigrostriatal degeneration in this model and the critical thresholds associated with the symptom appearance have been thoroughly investigated using several *in vivo* and post-mortem endpoints[63,64].

Anatomical quantification of the impact of MPTP administration in NHPs. We analysed the depletion of dopaminergic tissue in the 6 monkeys (M5, M6, M7, M8, M9, M11) that were involved in MI recordings after MPTP administration and in the experiments with the brain-controlled spinal cord neuroprosthesis. The monkeys were deeply anesthetized and perfused transcardially with a 4% solution of paraformaldehyde. Their brain was removed and stored at 4° C in 0.1 M phosphate-buffered saline azide (0.03%). We counted using an unbiased stereological method the nigrostriatal dopaminergic neurons and quantified the density of dopaminergic fibres in the caudate and ventral and dorsal putamen as described previously[65]. Briefly, tyrosine hydroxylase (TH) immunochemistry was performed using mouse anti-TH primary antibody (catalog MAB318, Millipore/Chemicon International, Technology, Billerica, MA, USA). Unbiased stereological counting of nigral TH^{ON} neurons as well as striatal optical density measurement were performed using Exploranova Mercator (Explora Nova, La Rochelle, France). Technical reasons prevented quantification of dopaminergic fibre density in M5 and of all brain tissues in M11.

NHP surgical procedures. All the surgical procedures have been described in detail previously[23,36]. Surgical interventions were all performed under full anaesthesia induced by atropine (0.04 mg kg^{-1}) and ketamine (10 mg kg^{-1}, intramuscular injection) and maintained under 1%–3% isofluorane after intubation. A certified functional neurosurgeon (J.B.) supervised all the surgical procedures. Surgical implantations were performed during one or two surgeries. M5-7 were implanted with a 96-channel microelectrode array (Blackrock Microsystems, 1.5 mm pitch) into the leg area of the left MI, and a wireless system[23,66] to record electromyographic signals (T33F-4, Konigsberg Instruments, USA) from the following leg muscles: gluteus medius (GLU), iliopsoas (IPS), rectus femoris (RF), semitendinosus (ST), gastrocnemius medialis (GM), tibialis anterior (TA), extensor digitorum longus (EDL), and flexor hallucis longus (FHL). M8-11 were implanted two 48-channel microelectrode arrays in the leg area of left and right MI, and a custom system that wired the electromyographic signals from right IPS, RF, ST, GM and TA; and left GM and TA muscles to a skull-mounted titanium pedestal. In a second surgery, two epidural spinal leads were inserted into the epidural space under the L2-L3 and L5–L6 vertebrae according to previously described methods[23,36]. We finely adjusted the rostro-caudal and medio-lateral position of the electrodes using intraoperative electrophysiological monitoring[23,36]. We anchored the implants to the spinous process of L3 and L6 vertebra with a suture. The wires of each spinal implant were routed subcutaneously to an implantable pulse generator (Activa RC, Medtronic Inc., USA) inserted between the intercostal muscles (see **Supplementary Information**). All the implantable devices were acquired from Medtronic, and research software reused from prior work. The proper location of the microelectrode arrays and epidural spinal leads with respect to gross anatomical landmarks was verified post-mortem in all the monkeys.

M9 was additionally implanted with two DBS mini-leads (4 contacts per lead, 0.5mm contact length, 0.5mm inter-contact distance, diameter 0.625mm, NuMED; USA) in the right and left subthalamic nucleus. Stereotactic coordinates of each subthalamic nuclei were calculated based on ventriculography, as detailed previously[67]. First, we attached a hollow cannula (inner diameter 0.625mm) to a stereotactic frame to insert the probe into the brain until the tip was located at the computed coordinates. We then descended the leads into the brain through the cannula. After the descent, we verified the proper location of each implant using X-ray. We then removed the cannula and fixed the lead to the skull using surgical cement. We again confirmed the location of each lead after fixation using X-ray, and then connected the leads with an implanted pulse generator (Activa RC, Medtronic, USA) using quadripolar extension cables (Medtronic, USA). We validated this

connection by recording stimulation artifacts following stimulation through each DBS contact. We confirmed the placement of DBS leads post-mortem using an MRI scan of the explanted brain.

The veterinary team continuously monitored the animals during the first hours after surgery, and several times daily during the seven following days. A few hours after surgery, the animals could move around and feed themselves unaided. We used clinical rating and monitoring scales to assess post-operative pain. Ketophen (2 mg kg^{-1}; subcutaneous) and Metacam (0.2 mg kg^{-1}; subcutaneous) were administered once daily. Lidocaine cream was applied to surgical wounds twice per day. The ceftriaxone sodium antibiotic (100 mg kg^{-1}; intramuscular) was given immediately following surgery, and then once daily for 7 days.

Design and fabrication of NHP epidural spinal leads. According to our earlier modelling work[20,21,24,36], in order to recruit the proprioceptive fibres that access motor neuron pools located in the L2-L7 spinal segments, EES needs to target the dorsal roots projecting to these segments. For this purpose, we tailored epidural spinal leads to the anatomy and physiology of the vertebral and spinal columns, taking into account the electrochemical requirements related to the size of the electrodes and interconnect tracts that are connected to the implantable pulse generator. To satisfy these limitations, we designed two implants: a rostral implant targeting the L2-L4 roots, and a caudal implant targeting the L5-L7 roots. The epidural spinal leads inserted in M8, M9 and M10 were produced by CorTec (Germany) using AirRay Electrode Technology. We also fabricated the epidural spinal leads using e-dura technology[32,33,68] (see **Supplementary Information** for details on the fabrication process), which was implanted in M11.

Data acquisition in NHPs. Procedures to record kinematics and muscle activity have been detailed previously[23,66,69]. We captured whole-body kinematics using the high-speed motion capture SIMI system (Simi Reality Motion Systems, Germany), combining 4-6 video cameras (100 Hz). We applied reflective white paint on the shaved skin of the animals overlying the following body landmarks: iliac crest (crest), greater trochanter (hip), lateral condyle (knee), lateral malleolus (ankle) and the fifth metatarsophalangeal (foot). We used the Simi Motion software (Simi Reality Motion Systems, Germany) to reconstruct the 3D spatial coordinates of the markers. Joint angles were computed accordingly. In M5-7, we used a custom-built system to receive the wirelessly emitted signals from the implanted T33F-4 devices (Konigsberg Instruments, USA). In M8-10, we used a W16 system (Triangle Biosystems, USA) to acquire the wirelessly transmitted signals. In M11, the implanted electromyographic system failed soon after the surgery. Consequently, all subsequent analyses were performed using kinematic recordings. We wirelessly recorded neural signals using the Cereplex-W system[23,28] (Blackrock Microsystems, USA). In M9, the skull-mounted pedestal used to connect the Cereplex-W system failed before we could test the efficacy of brain-controlled spinal cord stimulation on the ladder. Both electromyographic and neural wireless recording systems were connected to a Blackrock Neural Signal Processor (NSP, Blackrock Microsystems, USA) that synchronized electromyographic and neural signals sampled at 2kHz and 22kHz, respectively. The NSP band-pass filtered (500Hz-7.5kHz) the neural signals and extracted multiunit spikes as times when the signal crossed a threshold set to 3.5 times the root-mean-square of the signal[23]**.** This procedure resulted in spike times from each of the 96 electrodes. We used an additional NSP channel to record an analogue trigger of the SIMI system used to synchronize the SIMI video recordings with the physiological signals. The NSP continuously broadcasted Used Datagram Protocol (UDP) packets containing neural, multiunit spiking, electromyographic and trigger channel recordings over the local network. A dedicated storage computer received the UDP packets and saved the recordings on a hard drive.

Analysis of NHP gait and balance deficits resulting from MPTP treatment. In monkeys M1-9, we recorded gait kinematics before and after MPTP administration (**Supplementary Table 2**). We used two metrics as aggregate measures of performance: task time and crossing time. Similar to the instrumented Timed-up-and-go (iTUG) assessment used to evaluate motor capacity of people with PD[70,71], task time is the period from the moment the animal stands up on one side of a corridor or a ladder to the moment it places the food reward in its mouth on the other side of the corridor. Since task time may vary due to differences in the time each animal spent reaching for the food, we also calculated the crossing time as the period necessary for the animals to cross the central portion of the corridor or ladder. To quantify locomotor performance, we applied a PC analysis on 83 gait parameters (**Supplementary Table 3**) calculated based on previously described methods[23,36,69]. We used three leading PC of the space spanned by these parameters to visualize the differences between the gait cycles recorded before and after MPTP administration, or across the experimental conditions (**Extended Data Fig. 1**). Next, we extracted the factor loading on each PC to identify the parameters that more robustly explained the differences between the conditions.

Analysis of gait impairments of people with Parkinson's disease. To compare gait deficits of people with PD to the gait deficits recorded from our MPTP non-human primate model, we organized gait recordings in people with PD and healthy controls as part of the PREDI-STIM clinical study (NCT 02360683). The PREDI-STIM study was approved by the Nord Ouest-IV Ethical Committee (2013-A00193-42) and was conducted in accordance with the Declaration of Helsinki. The inclusion criteria involved patients with Parkinson's disease receiving a pre-therapeutic assessment and monitoring for one, three and five years as part of the regular monitoring of the subthalamic nucleus deep brain stimulation. The study involved one or more sessions during which we recorded full-body kinematics of the study participants.

Under the framework of the PREDI-STIM study, we recorded and analysed gait of N = 25 participants diagnosed with Parkinson's disease, exhibiting debilitating gait deficits with various degrees of severity, and N = 9 age-matched healthy controls. We recorded whole-body kinematics using a Vicon motion-capture system (Vicon, Oxford, UK). We attached 34 reflective markers (26 on the legs, arms and trunk, and 8 on the head and wrists) on the surface of the skin of the participants to cover all key body joints (foot, ankle, knee, hip, shoulder, elbow, hand, neck and head, as well as spinal vertebrae T10 and C7). We employed the Nexus biomechanical software (Vicon, Oxford, UK) to triangulate the centroid of each joint in each time point. Putting the joints centroids together provided us with a full-body kinematics. We developed a custom software in the MATLAB environment (The MathWorks, Inc., USA) to derive the timing of gait events (heel strike / foot off) and calculate the walking parameters from full-body kinematics. We then used this software to discretize each gait-cycle into N = 65 kinematic variables, which quantified the amplitude, speed or consistency of each step. To enable comparisons with non-human primate results, we restricted our analyses to the 35 kinematic variables related to leg movements (**Supplementary Table 5**). We then applied the principal component analysis on this high-dimensional representation of gait across Parkinsonian and healthy study participants to identify the most relevant variables to explain changes in walking induced by the Parkinson's disease, and potential improvements that can be brought in by a therapy.

Identifying the hotspots from spatiotemporal maps of motor neuron activity. Video recordings were used to mark the right foot strike and right foot off gait events, and thus calculate the average proportion of the stance and swing phases over all collected gait cycles. We transformed the electromyographic signals into activity of motor neuron pools on using previously described methods[23,36]. The activity of motor neurons during each gait cycle was converted from time to gait

phase coordinates (see **Supplementary Information**). We then generated the spatiotemporal maps of motor neuron activity by averaging the activity of motor neurons over all the recorded gait cycles. We applied a Gaussian Mixture Model to these maps to identify the dominant hotspots of activity[72].

Decoding of hotspot initiation events from MI neural activity of MPTP-treated NHPs. We implemented an algorithm that decoded the initiation of weight acceptance and leg lift hotspots from the neural activity. We used datasets with synchronized multiunit spikes and gait events to calibrate the decoding algorithm, as done previously[23,33,36] and described in detail in the Supplementary Information. Briefly, we used the spatiotemporal maps of motor neuron activity to calculate the average temporal difference between the right foot off and foot strike gait events and the right weight acceptance and leg lift hotspot initiation events, respectively. We used these latencies to transform gait events into weight acceptance and leg lift hotspots initiation events. In the same dataset, we estimated multiunit spike rates in each of the 96 channels by summing up the multiunit spikes with a 150 ms history every 0.5 ms. We used these multiunit rates and the hotspot initiation events to calibrate a multiclass rLDA decoder[23,33,35,36]. Based on a 300-500 ms history of neural activity, the decoder returned the probabilities of observing each of category of hotspot initiation events used to calibrate the decoder. The hotspot event types included: (i) left weight acceptance, (ii) left leg lift, (iii) right weight acceptance, and (iv) right leg lift. When the probability of one of the hotspot initiation events crossed a threshold of 0.8, that event was detected. To verify the efficacy of our decoding approach after MPTP administration, we used the dataset collected from M6 and M7, and performed offline cross-validation of our decoding approach. We measured the temporal accuracy of the decoder in 9 (M6) and 8 (M7) sessions performed before and after MPTP administration.

Decoding of hotspot initiation events from epicortical signals of people with PD. We analysed data of participants P2 and P3 of the “Motor Network in Parkinson's Disease and Dystonia: Mechanisms of Therapy” clinical trial (clinicaltrials.gov ID: NCT03582891). Study was previously described in detail[46]. In short, the participants provided written consent in accordance with the IRB and the Declaration of Helsinki. They were recruited from a population referred for implantation of deep brain stimulators for PD. Before recruitment, they were evaluated by a movement disorders neurologist and met diagnostic criteria for PD[73] and by a neuropsychologist to exclude major cognitive impairment or untreated mood disorder. Inclusion criteria included motor fluctuations with prominent rigidity and bradykinesia in the off-medication state, baseline off-medication MDS-UPDRS-III scores between 20 and 80, greater than 30% improvement in MDS-UPDRS-III on medication than off of medication and absence of significant cognitive impairment (score of 20 or above on the Montreal Cognitive Assessment). The full IDE application (G180097) and study protocol have been shared with other researchers via the Open Mind initiative (https://openmind-consortium.github.io).

Study participants underwent bilateral placement of cylindrical quadripolar deep brain stimulator leads into the subthalamic nucleus (Medtronic model 3389; 1.5-mm contact length and 2.0-mm intercontact spacing), bilateral placement of quadripolar cortical paddles into the subdural space over the cortical area that included the motor cortex (Medtronic model 0913025; 4-mm contact diameter and 10-mm intercontact spacing) and bilateral placement of investigational sensing IPGs in a pocket over the pectoralis muscle (Medtronic Summit RC+S model B35300R). The IPG on each side was connected to two leads by 60-cm lead extenders (Medtronic model 37087). The Summit RC+S IPG is a 16-channel device that, through the use of its application programming interface, allows researchers to record four bipolar time domain channels (250/500 Hz) or two channels at 1,000 Hz[74,75]. For all research functions, including configuring and initiating sensing and developing

embedded or distributed adaptive DBS, investigators controlled the device by writing software in C# within the device API, accessed using a 'research development kit' (RDK; Medtronic model 4NR013) provided by the manufacturer. We wrote a software application to configure and initiate streaming data from two RC+S devices simultaneously (available at https://openmind-consortium.github.io). This software is written in compliance with the FDA code of federal regulation CFR 820.30, which specifies design controls for implantable human devices.

Here, we have analysed recordings collected with P2 and P3 during one session of overground walking in a corridor, and with P2 during one session of walking on a treadmill. In those sessions, the participants were on their regular levodopa therapy and their DBS was kept off. Cortical field potentials were sampled at 500 Hz. We simultaneously recorded video using a camera and full body kinematics using a set of IMU sensors distributed across major anatomical landmarks.

The feature selection and decoding were performed according to previously published procedures[23,33,35,36,38,45]. Briefly, we used the reconstructed kinematics of the ankle to identify left and right leg lift hotspot initiation events. These events match the events used to synchronize the spinal stimulation with the movement intentions of non-human primates. We processed the epicortical signals using a high-pass filter at 0.5Hz and then lowpass filtered with a 2nd order 0.25s long Savitzky-Golay filter[38,76]. The synchronized dataset of processed epicortical signals and gait events was then used to calibrate two rLDA decoders targeting respectively left and right leg lift hotspot initiation events. We evaluated the offline decoding accuracy for each side separately by performing cross-validation of the decoders (see **Decoding performance**).

Decoding performance. We derived the distribution of temporal differences between the decoded hotspots initiation events and the hotspots initiation events reconstructed from video recordings. We then quantified the performance of our decoders using temporal decoding accuracy, defined as the proportion of temporal differences falling within a window of 200 ms. Standard error was estimated using bootstrapping with 10 000 resamples.

Therapeutic approach. We aimed to re-establish the natural dynamics of motor neuron activation using EES protocols targeting the weight acceptance, propulsion and leg lift hotspots associated with the leg and right legs. This concept implied that EES had to (i) be triggered at the appropriate locations with amplitudes that reproduce the activation of these hotspots (ii) at the times when those hotspots should be active and (iii) for the duration over which each hotspot is activated. The following three sections describe how we achieved these three requirements.

Identification of amplitude and duration to target each hotspot. In M8-10, we recorded the electromyography from right leg muscles in response to single-pulses of EES. For each of the 16 electrodes of the spinal implant, we recorded the muscle responses over a broad range of stimulation amplitude, ranging from sub-threshold to saturation. We translated these recordings into a mapping between each electrode, EES amplitude, and evoked muscle responses. We transferred the relative amplitude of the observed responses into spatial maps of motor neuron activity. We then identified the optimal combinations of electrodes and amplitudes that maximized the correlation between the targeted and elicited spatial map of motor neuron activity. Correlations were measured at the centre of each hotspot. We thus obtained three combinations of electrodes and amplitudes that targeted the weight acceptance, propulsion and leg lift hotspots. Since we recorded only two muscles on the left side, we could not follow the same procedure to determine EES protocols for the left hotspots. Consequently, we determined these combinations based on the observed kinematic responses to single-pulse stimulation. This procedure was applied for both sides in M11, since muscle activity could not be recorded in this animal. EES durations were set to the duration of the corresponding

hotspots. In M11, the durations were determined by observing kinematic responses to stimulation during locomotion. We thus defined a set of "stimulation protocols" – combinations of stimulation location, amplitude and duration designed to reinforce a specific hotspot.

Using detected hotspot initiation events to trigger spinal stimulation. We designed a real-time control system that used the decoding algorithm to trigger EES protocols at appropriate times. The control computer was connected to the local network and continuously received used datagram protocol (UDP) packets containing neural recordings. We developed a C++ software application (Visual Studio 2010, 2015) running on the control computer, which analysed the neural signals in real-time. Every 15 ms, the application used the decoding algorithm to calculate the probabilities. If one of the hotspot initiation events was detected, the application triggered the relevant EES sequence. We designed EES sequences as composite stimulation protocols that reinforce one or more of the ongoing or soon-to-be-active hotspots. Since these hotspots often overlapped, the sequences executed protocols in parallel to reinforce the natural dynamics of motor neuron activity. The wireless control of the stimulation had a mean transmission latency of 105 ms[23]. We accounted for this latency when translating gait events into hotspot initiation events (see **Extended Data Figure 5a**).

Tuning of EES sequences using brain-controlled spinal cord neuroprosthesis. Once the decoder was calibrated, we used the detected hotspot initiation events to trigger EES sequences that contained only one of the 6 protocols derived from the optimal combinations of electrode and amplitude targeting each hotspot. The animals walked while the brain-controlled spinal cord neuroprosthesis triggered these simple EES sequences. We then tuned the amplitudes and durations of EES protocols based on muscle and kinematic responses. We performed this procedure for all six protocols. We then designed "left" and "right" composite EES sequences containing either: (i) left weight acceptance, right leg lift and left propulsion protocols, or (ii) right weight acceptance, left leg lift and right propulsion protocols, respectively. We then used the detected left or right weight acceptance events to trigger these sequences. To account for interaction of multiple EES protocols, we tuned the design of these composite EES sequences until we reached satisfying behavioural responses. This tuning process typically lasted for about an hour during the first session. Subsequent sessions required only minor tuning that typically lasted 5 to 10 min.

Calibration procedure to account for stimulation-induced changes in neural signals. Due to sparsity of EES bursts using only one hotspot event (once over a 1-2s long gait cycle), the neural activity used to decode hotspot initiation events was not affected by the motor cortical response elicited by bursts of EES[23]. However, the repeated delivery of EES sequences that reinforce all six hotspots disrupted the decoder. We thus developed a procedure to ensure that the decoder would remain reliable during EES despite cortical responses to EES bursts. For this purpose, we implemented the previously-developed two-step calibration procedure[23], which we optimized for PD. Briefly, once we tuned the composite EES sequences, we recorded several trials along the corridor while only the left or right weight acceptance events triggered left or right composite sequence, respectively. We then calibrated a second decoder based on the data recorded without and with EES. This two-step decoder successfully compensated for stimulation-induced changes in motor cortex activity (see **Extended Data Figure 5b**).

Evaluation of the brain-controlled spinal cord neuroprosthesis In NHPs after MPTP administration. We evaluated the therapeutic efficacy of the brain-controlled spinal cord neuroprosthesis to alleviate gait and balance deficits in M8, M9 and M11. We applied all the above procedures to calibrate the decoder and tune EES protocols. In M8, the decoders used in both

reported sessions were calibrated using the data recorded one or two days before. The same decoder was used to deliver EES sequences during locomotion along the ladder. We measured locomotor performance using task and crossing time, as explained above. M8 and M11 showed specific deficits. M8 developed occasional episodes of slowing of gait and freezing-of-gait. M11 displayed frequent falls when progressing along the ladder. To evaluate the improvement in these specific deficits with the neuroprosthesis, we calculated the proportion of trials along the corridor that contained episodes of slowing of gait or freezing-of-gait in M8, and the proportion of trials along the ladder in which M11 fell. We also quantified the impact of the neuroprosthesis on kinematics and muscle activity. We isolated all the gait cycles where all four decoded hotspot initiation events were within a window of 200ms with respect to the reconstructed hotspot initiation events. In M8 and M9, we compared locomotor performance with and without using the neuroprosthesis for two different days of recordings before the MPTP administration as a reference to its healthy gait. We compared the effect of the neuroprosthesis on the variables that were identified as most relevant to account for gait and balance deficits resulting from MPTP administration: stride length, endpoint velocity of the foot and lateral hip displacement in the corridor task; and stance duration and velocity in the ladder task. In M8 and M9, we applied a PC analysis on 83 gait parameters calculated for each gait cycle and visualized the impact of the experimental conditions in the plane defined by the first two PC, according to previously described methods[23,36,69]. To quantify gait performance, we calculated the mean Euclidean distance between gait cycles in the entire 83-dimensional space of kinematic parameters as described previously[23,69] and above.

Evaluation of the synergistic effects of brain-controlled spinal cord neuroprosthesis and DBS therapies in NHPs. We equipped monkey M9 with both the neuroprosthesis and DBS to evaluate how the neuroprosthesis complements the effects of the DBS therapy. We first tuned and tested the neuroprosthesis therapy as described above, followed up by tuning and testing the effects of the DBS therapy and, finally, testing the two therapies together. To tune the DBS, we applied charge-balanced biphasic stimulation pulses (90 μs, 125 Hz, constant voltage mode) using each DBS contact at increasing amplitudes in steps of 0.2V. We increased the amplitude until we observed stimulation-induced motor responses (e.g. neck twitches) while the animal was sitting. We then reduced the amplitude, typically by 0.1 – 0.4V, until these motor responses disappeared. To evaluate the effects of DBS, we turned on the stimulation at least 30 minutes before the experiments started to account for reported slow dynamics in the effects of DBS on gait[7]. When evaluating 20Hz DBS, we increased the stimulation amplitude to compensate for frequency-related changes in induced charge according to previously published guidelines[77]. The motor changes induced by DBS additionally included observations in free behaviour of the animal, which we quantified in terms of (i) number of corridor crossings within a ten-minute interval, (ii) number of corridor crossings completed without stopping, and (iii) average gait cycle duration during each crossing. These quantifications aimed to account for improvements in mobility and awareness, facility to turn and ambulate, and locomotor speed.

STIMO-PARK study design and objectives. The experiments to evaluate the spinal cord neuroprosthesis were carried out as part of the ongoing clinical feasibility study STIMO-PARK (clinicaltrials.gov ID: NCT04956770) that investigates the effects of lumbosacral EES to improve mobility in people with Parkinson's disease. The STIMO-PARK study was approved by the Swiss ethical authorities (Swissethics protocol number 2021-0047) and the relevant regulatory authorities (Swissmedic protocol 100008) and is conducted following the Declaration of Helsinki. The inclusion criteria include idiopathic Parkinson's disease with III-IV Hoehn-Yahr stage, exhibiting severe gait

difficulties and postural instability, use of the Medtronic DBS implant and receiving medication for Parkinson's disease. The study involves assessments before the implantation surgery for the spinal EES neurostimulation system, the surgical implantation of the neurostimulation system, a 1-month period for configuration of EES protocols and sequences, and a 3-month period of physiotherapist-assisted rehabilitation during 3-hour sessions taking place 2 to 3 times per week. At each of the sessions, P1 reported on the duration of the use of the neuroprosthesis. The rehabilitation program is personalized based on the participants' needs and improvements.

P1 participant of the STIMO-PARK study. P1 was enrolled in the STIMO-PARK study by signing a written informed consent. He provided written informed consent for publication of identifiable images and video. He was a 61-year-old male at time of enrolment. He has been diagnosed with Parkinson's Disease at the age of 36 and implanted with DBS at the age of 44. He is currently in stage 3 of the Hoen-Yahr scale. He experiences fluctuations in his gait pattern and lower limb symptoms typical of later stages of PD, including slowness, asymmetry, rigidity, small steps, flexed posture. Before being implanted with the EES system, during the 6-minute walk test P1 was able to cover 433 meters with DBS turned on and during his regular levodopa intake, and 224 meters with DBS turned off and with the last levodopa intake the evening before. His MDS-UPDRS motor examination scores (part III) in these two states were 20 and 47, respectively. He started to experience freezing-of-gait over the last decade, which greatly impacted his independence and quality of life. Before participation in the study, he reported 4 falls per day on average due to freezing-of-gait. Following the enrolment, we performed a CT scan of his torso and a structural MRI scan of his spine to generate a personalized anatomical model of his spine. Following the pre-surgical assessments, P1 was implanted with the spinal EES neurostimulation system. After the surgery, P1 was transferred to the neurosurgery ward for recovery. P1 then went back to the hotel for a one-week recovery period. After recovery, we successfully configured the EES protocols and sequences for P1 during the study configuration period. This study presents the analysis of seven sessions recorded during the study configuration period after the EES protocols and sequences have been configured. P1 continued with the study procedures afterwards. All surgical and experimental procedures were performed at the Lausanne University Hospital (CHUV). The procedures are described in detail below.

P1 personalized neurobiomechanical model. In order to estimate the target for the immediate effects of our therapy, we sought to simulated the gait of P1 given his anatomy but in the absence of neurodegeneration. To this end, we generated a personalized musculoskeletal model of P1 by adapting the Lower Limb model[78] to P1's anatomy and by optimizing the reflex-based gait controller used to generate walking[79]. Similar methods have been used to reproduce gait of healthy individuals[80], gait of elderly affected by the muscle weakness and reduced contraction speed[81], and gait adaptations due to ankle plantarflexor muscle weakness and contracture[47,79]. The musculoskeletal model included three planar degrees of freedom at the pelvis and another three for each leg: hip flexion, knee flexion and ankle flexion. These degrees of freedom are actuated by eight Hill-type muscle-tendon units[82] per leg corresponding to eight different leg muscles: (1) gluteus maximus, (2) hamstring muscles, (3) iliopsoas, (4) vastus muscles, (5) biceps femoris, (6) gastrocnemius, (7) soleus, and (8) tibialis anterior. This model is scaled to P1 morphology derived from the motion tracking of P1 while standing using the OpenSim scaling tool[83]. We also scaled the muscular properties of the model using muscles' cross-sectional area segmented from P1's thigh CT scan. As the maximal voluntary force and cross-sectional area are significantly correlated through aging[84], we scaled the maximal isometric force of each Hill-type muscle-tendon unit to the ratio of

the muscle cross-sectional area over the healthy reference from[85,86]. Due to the absence of the calf CT scans, we scaled the maximal isometric force of the calf muscles using the mean of the thigh muscle ratios. To obtain a more robust estimate of the muscle strengths, we averaged the scaling over both sides. The resulting scaling factors were 0.65 for the hamstrings group, 0.87 for the quadriceps group and 0.76 for the calf group. We then used the SCONE software[87] to optimize the parameters of the reflex-based gait controller[79]. This controller is composed of phase dependent reflexes providing muscle excitation based on muscle length, velocity or force feedback. We simulated P1 gait in the absence of neurodegeneration using Covariance Matrix Adaptation Evolutionary Strategy[88] to optimize the controller parameters. We used a cost function penalizing falling, muscles' metabolic cost[89], joint angles out of healthy ranges and the head balance, with respective weights 100, 0.1, 0.1 and 0.05 balancing the competitive objectives. About 500 generations of CMA-ES were necessary to reach a stable gait initialization[79]. Once the parameters of the controller have converged, we generated 200 steps of this neurobiomechanical model and extracted full kinematics of lower limbs and muscle activity. We then compared these simulation-generated kinematic and muscle activity signals with the signals recorded during the P1 study sessions.

Planning the surgical placement of the epidural spinal lead in P1 using personalized anatomical model of the spine. We used the P1's CT and MRI scans to generate a three-dimensional anatomical model of his spine. First, we segmented the vertebral bones from the CT scan using a convolutional neural network (CNN) based framework[90] trained on the VerSe datasets[91]. We then segmented the spinal cord tissue from the MRI scan using a nnU-Net[92] after pre-processing and with post-processing using the Spinal Cord Toolbox[93]. Remainder of the lead placement planning was performed in the Sim4Life software. We loaded the MRI scan images and the segmented spinal cord tissue and then identified the locations where spinal cord roots merge with the spinal cord, hereafter termed root merging point. We then generated the trajectories of the spinal cord roots that follow the path from the root merging point to the entry of that root into the spinal canal. We defined the spinal cord segments as spinal cord tissue bounded by the midpoints between the two neighbouring root merging points. We defined the root trajectory leading to the root merging point as the central rootlet and distributing four off-centre rootlets across the segment. We then loaded the vertebral bones and disks segmented from the CT scan and aligned it to the spinal cord and roots. We then used this combined anatomical model to propose a placement of the lead. We first loaded a 3D model of the lead and placed it centred over the dorsal side of the spinal cord covering most of the L1-L5 spinal segments, which control the contraction of leg muscles. Position of the lead with respect to the segmented vertebral column determined the insertion point of the lead to be between L1 and T12 vertebra.

Surgical implantation of the STIMO-PARK investigational spinal EES neurostimulation system in P1. During the surgery, we implanted P1 with a Specify® SureScan® MRI 5-6-5 16-electrode epidural spinal lead (Medtronic plc, Fridley, MN, USA) in the posterior epidural space covering the lumbar spinal cord segments. This lead is clinically approved for the treatment of chronic pain. We then connected the lead by a cable to an Activa™ RC IPG (Medtronic plc, Fridley, MN, USA), which is clinically approved as an IPG for deep-brain stimulation therapy. The IPG was first inserted into a subcutaneous pocket in the abdomen. The lead cables were then tunnelled from one opening to the other and connected to the IPG. These combined elements and associated firmware constitute an investigational spinal EES neurostimulation system that was tested as part of this clinical study.

We identified the insertion level during surgery using fluoroscopy. To insert the lead, we performed an approximately 5 cm midline skin incision. We opened the fascia and the muscles retracted bilaterally. Excision of the midline ligamentous structures and T12/L1 flavectomy and partial laminectomy enabled the insertion of the lead into the spinal epidural space. To perform the insertion, we placed the lead over the midline of the exposed dura and advanced rostrally to the target location. We used the ISIS XPress monitoring and stimulation system (inomed Medizintechnik GmbH, Emmendingen, Germany) to accurately adjust the medial and segmental position of the lead. To this end, we delivered EES pulses with a pulse width of 300μs at 0.5 Hz and at increasing amplitudes to elicit muscle responses that were recorded with subdermal (Neuroline Twisted Pair Subdermal, 12 x 0.4 mm, Ambu A/S, Balle- rup, Denmark) or intramuscular needle electrodes (Inomed SDN electrodes, 40 mm, inomed Medizintechnik GmbH, Emmendingen, Germany). The lateral position of the lead was adjusted so that the bottom electrodes selectively recruit the calf muscles while maintaining good activation of the hip flexor muscles using the top electrodes. The medial position of the lead was adjusted to reach a similar side-specific muscle recruitment with the corner electrodes. The final location of the lead overlaid lumbar and upper sacral segments. The surgery then finished and P1 was transferred to the neurosurgery ward for recovery.

Reconstruction of the electrode position with respect to the patient spine was assessed from the post-operative CT scan. CT images enabled reconstructing the three-dimensional geometry of vertebral and the location of the lead electrodes inside the vertebral column. The resulting 3-dimensional volume reconstruction of the spinal cord of the participant included the lead with its electrodes, vertebral bodies, white matter, trajectory of dorsal spinal roots and rootlets.

P1 spinal cord neuroprosthesis. We delivered the EES of the lumbar spinal cord by controlling the delivery of current though the 16 IPG header channels, each connected to one of 16 electrodes of the epidural spinal lead, or through the IPG case. The IPG was modified from its clinical version with an investigational firmware that enabled real-time communication with a NEUWalk Research Programmer Application software (NRPA, Model 09103, Medtronic) running on an external computer. The NRPA acted as a relay between the G-Drive Plus control software (described below) and the IPG. The NRPA communicated wirelessly with the IPG through the following communication chain: the NRPA sent commands via a virtual COM port corresponding to a Bluetooth adapter, a custom wireless bridge consisting of a nano computer (Raspberry Pi) received this command and forwarded it to a virtual COM port corresponding to a USB adapter, a USB to infrared adapter (ACT-IR224UN-LN115-LE, ACTiSYS Corporation, Fremont, CA, USA) transformed this command into infrared signals that were then read by a modified Medtronic patient's programmer (Sensing Programmer Telemetry Module SPTM, Medtronic), which finally transmitted the command to the patient's IPG by electromagnetic induction through the skin.

G-Drive Plus software for configuration and control of the spinal cord neuroprosthesis in P1. We developed a custom G-Drive Plus software application to configure and control the spinal cord neuroprosthesis[25]. G-Drive Plus runs on a desktop computer, laptop or tablet and interfaces with the stimulation system (through NRPA) and collects the signals from different sensors that can be used for closed-loop stimulation. The sensors include the wireless Next Generation Inertial Measurement Units (NGIMU; x-io Technologies Limited, UK) and the Trigno® Research+ System utilizing wireless Trigno® Avanti sensors that can record both the IMU and EMG signals simultaneously. G-Drive Plus includes a graphical user interface (GUI) that enables rapid personalization of EES protocols, each of which is parametrized by a set of cathodes and anodes to deliver the stimulation, the amplitude of the stimulation current and the stimulation frequency. G-Drive Plus GUI also includes a stimulation

scheduler that enables rapid personalization of sequences of EES protocols. Once defined, these EES protocols and sequences can be uploaded to the IPG. To enable closed-loop controlled stimulation, the execution of EES sequences is linked to specific events detected from data collected by the sensors. On detection of an event, G-Drive Plus sends wireless command to the IPG to execute the linked sequence. After 105ms on average, the currently running stimulation sequence is interrupted and the commanded sequence is initiated. The following command can only be sent after 200ms on average, once the IPG has send back the confirmation that the previous command has been received and executed. G-Drive Plus can also trigger acquisition from video cameras and emit standardized synchronization pulses. During recording sessions, these functionalities allow us to use G-Drive Plus to visualize and immediately assess the effects of the EES protocols and EES sequences on muscle activity and whole-body kinematics. All the acquired data, including the delivery of EES protocols synchronized with the kinematics and muscle activity is saved for offline analysis.

Calibration of EES protocols in P1. In an EES calibration session, we used single-pulse EES to identify electrode configurations that recruit the six targeted hotspots of spinal activity: left and right weight acceptance, propulsion and leg lift hotspots. Weight acceptance roughly corresponds to knee extension, propulsion to ankle extension, and leg lift to coactivated hip flexion and ankle flexion, respectively. The participant was lying relaxed in supine position on an examination table. We recorded EMG activity from left and right iliopsoas (Il), rectus femoris (RF), vastus lateralis (VLat), semitendinosus (ST), tibialis anterior (TA), medial gastrocnemius (MG), and soleus (Sol) muscles using Delsys Trigno wireless EMG sensors (Delsys Incorporated). We applied the Nuprep abrasive paste on the skin (Weaver and Company, Aurora, CO) to reduce electrode-skin resistance and improve EMG signal quality. We then mapped the muscle responses to single-pulse EES (300 μs pulse width) delivered using monopolar configurations (one lead electrode as cathode and case as anode) at currents ranging from 0.1mA to 3.5mA. We systematically tested all possible monopolar configurations. For each configuration, the EES current was gradually increased until all muscle responses reached saturation or until P1 reported discomfort. We recorded 3 repetitions for each amplitude. We then used recorded EMG responses to compute spinal map activations for each monopolar configuration across a range of amplitudes. We then identified eight monopolar configurations that each generate a spinal map activation with the highest correlation with one of the identified hotspot spinal activations. If the muscle activation selectivity of one of these configurations was not satisfactory, we refined that EES protocol with multipolar electrode configurations, which use additional anodes to steer the electrical field towards the targeted posterior roots. We then tuned the frequency and amplitude of each of the EES protocols. Since our intention was to finally generate EES sequences with multiple overlapping EES protocols, the limitation of the Activa RC IPG allowed the use of only a single stimulation frequency. Extensor muscles are more responsive to low-frequency stimulation (e.g. < 40 Hz), while the flexor muscles respond better to higher frequencies (e.g. > 80 Hz). Since our EES protocols targeted both the flexor and extensor muscles, our tuning identified 60Hz as the most effective stimulation frequency overall. We then tuned the current amplitude for each EES protocol by asking the participant to walk while triggering that protocol and observing the muscle responses. We selected the amplitudes that generated a clear enhancement of gait and were below the P1‘s discomfort threshold. We found that continuous stimulation using both the left and the right knee extension EES protocols clearly enhances the gait. We therefore defined two of left and right knee extension EES protocols, a knee extension “boost” EES protocol with a higher amplitude to coincide with the natural activation of the knee extension hotspot, and

another with a lower amplitude active during the remainder of the gait cycle (**Supplementary Table 6**).

Calibration of EES sequences in P1. In an EES calibration session, we assembled the EES protocols into two EES sequences: “Left Foot Off” and “Right Foot Off”. These were designed to be initiated in synchrony with the beginning of the left and right leg lift hotspot, respectively. We tuned the duration of each protocol in the sequence by asking P1 to walk overground while we delivered the EES sequences. We used G-Drive Plus to look at the overlap of EES protocols and activation of muscles targeted by those protocols. We modified the sequences until all the misalignments were removed (**Supplementary Table 7**). With non-human primates, whose gait cycle typically lasted more than one second, we used four EES sequences. With the help of EES, the gait cycle of P1 was often below 0.8 seconds. Due to the communication chain between G-Drive Plus and the IPG, we can only send one command to the IPG every 200ms, Therefore, using more than one EES sequence per side generated delays in the execution of EES sequences, which made the neuroprosthesis ineffective.

P1 corridor and freezing circuit sessions. These sessions tested the synergistic effects of DBS and EES therapies through four conditions: DBS off EES off, DBS on EES off, DBS off EES on, and DBS on EES on. Since the effect of DBS takes time to washout, we could only test either the DBS off or DBS on conditions in a single session. For the DBS off sessions, we instructed P1 to turn his DBS therapy off in the morning before the session. P1 maintained the same daily regime of levodopa intake during the trial protocol. To ensure balanced comparison between the conditions tested on different days, sessions always stated at the same time, thus ensuring roughly the same levedopa levels at the beginning of each session. During these sessions, we first equipped P1 with up to 16 wireless Trigno® Avanti sensors with bipolar surface electrodes over the muscles of left and right legs: iliopsoas, rectus femoris, adductors, vastus lateralis, semitendinosus, tibialis anterior, medial gastrocnemius, and soleus. In addition, we attached two NGIMU sensors on the surface of the left and right shank. Additionally, we attached 14 infra-red reflective markers on the following anatomical landmarks: left and right toe, ankle, knee, hip, shoulder and two on each wrist. For the remainder of these sessions, P1 walked within the instrumented space of our gait laboratory as we recorded his EMG activity and kinematics and controlled his spinal EES. We acquired the EMG and IMU signals using the Trigno® Avanti sensors with a 1259 Hz and 148 Hz sample rate, respectively, and additional IMU signals from NGIMU sensors at 30 Hz. We obtained the kinematic recordings using a Vicon 3D motion capture system (Vicon Motion Systems, Oxford, UK), consisting of 14 infrared cameras, each set to record the reflection of infrared-reflective markers at 100 frames per second. The Vicon system covered a 12 m x 4 m x 2.5 m workspace. We also captured chronophotographic images of participants using a high-definition camera (FUJIFILM X-T2, 5 images/s, ISO 6400, shutter speed 1/250 sec). As he walked, P1 was always followed by a physiotherapist to prevent falls in the case of freezing. During the corridor sessions, on the mark of the experimenter, we asked P1 to stand up from his chair, walk from before one floor marker to beyond another floor marker in a straight line, turn around and come back again in the straight line, and repeat this the second time. Once he finished the task, P1 was free to sit down and rest. We defined an epoch stating with P1 passing the marker on one side of the Gait lab and ending with P1 passing the marker on the other side of the Gait lab as a trial. We defined the time to complete a trial as task time. The epoch between the P1 standing to walk on experimenter’s mark and him finishing the task was defined as a “trial set”. During the freezing circuit sessions, we built a circuit consisting of narrow corridors with obstacles. On the mark of the experimenter, we asked P1 to stand up from his chair and walk across the floor marker

and through the circuit across the obstacles until he reached the floor marker on the other side of the Gait lab. Once he finished the task, P1 was asked to walk around the circuit to the initial position, sit down and rest. We defined each crossing of an obstacle as a trial, during which P1 either froze or not. We defined one passing of the entire circuit as a trial set. In both types of sessions, P1 and the physiotherapist were not informed on whether the EES was on or off during that trial set. In the corridor sessions, after each trial, we asked P1 to comment on and score the quality of his gait on a scale from 0 to 5 with 0.25 increments. After P1 finished with the scoring, we asked the physiotherapist to also comment on and score the quality of P1's gait on the same scale.

Kinematically-controlled spinal cord neuroprosthesis in P1. Process to calibrate the closed-loop control of EES for P1 followed the procedure based on our earlier work to decode sparse events from motor cortical spiking activity in non-human primates[23,33,36] and people[35], from motor cortical ECoG activity in people[38,45], and employed earlier in the study for the non-human primates and people with PD (**Extended data Figure 5**). On a day preceding the first overground walking session, we recorded a dataset in which P1 walked straight while being equipped with the NGIMU sensors, Trigno® Research+ system and recorded by cameras. He walked first in the DBS on EES off condition. We used these trial sets to calibrate thresholds on the pitch angles acquired from the NGIMU sensors positioned on the left and right leg shanks. We then asked P1 to again walk straight, now in the DBS on EES on condition where the Left Foot Off and Right Foot Off EES sequences were triggered by left and right leg shank pitch angles respectively passing their thresholds. We then labelled the gait events of both the DBS on EES off and DBS on EES on dataset using a custom-developed Matlab® program through visual inspection of the video frames. We used these labelled datasets to calibrate rLDA decoders that detected the initiation of the left leg lift and right leg lift hotspot initiation events. Decoder used accelerations and angular velocities acquired by the Trigno® Avanti sensors lowpass filtered with a 2nd order 0.25s long Savitzky-Golay filter[38,76] as inputs. To enable closed-loop control of EES sequences in real-time, we developed a DecodingGate C++ software application (Visual Studio 2010, 2015, 2017) that acquired the Trigno® Avanti sensors recordings from G-Drive Plus, processed those recording, applied the rLDA decoding algorithms, and, upon detection of hotspot initiation events, sent the commands to the G-Drive Plus to initiate the relevant EES sequence. G-Drive Plus then relayed these commands to the IPG. Decoding Gate ran on a separate computer and exchanged data with G-Drive Plus via UDP packets through a local network. While calibrated from data recorded during straight walking in the DBS on conditions, the decoders remained accurate in the DBS off conditions, and when used in the freezing circuit task (**Fig. 5-6**).

Assessment of gait impairments in P1. After each corridor trial, the physiotherapists attributed a general gait quality score according to predefined criteria (**Supplementary Table 8**). We processed the motion tracking of P1's legs into kinematic variables that were used to quantify key deficits of Parkinsonian gait. We quantified gait speed by task time and stride length, and gait asymmetry for temporal and spatial parameters by the ratio of gait phases and step lengths between left and right legs[94]. Gait is more symmetric as these ratios approach zero.

$$Gait\ Phase\ asymmetry = 100 \times \left| \log \left(\frac{\frac{Swing\ duration_R}{Stance\ duration_R}}{\frac{Swing\ duration_L}{Stance\ duration_L}} \right) \right|$$

$$Step\ length\ asymmetry = 100 \times \left| \log \left(\frac{Step\ length_R}{Step\ length_L} \right) \right|$$

We also quantified the variability of gait patterns using stride time coefficient of variation, which has been associated to gait instability and risk of fall in PD[95,96]. The coefficient of variation is defined as the ratio between the standard deviation and the mean, and increases with variability.
We quantified the gait upper body control by measuring the arm swing angle[95].

Assessment of balance problems in P1. We evaluated the impact of the spinal cord neuroprosthesis and DBS therapies on balance problems by using the standard Mini-BESTest clinical evaluation[97], and using the Activities-specific Balance Confidence (ABC) scale questionnaire[98-100].
Assessment of freezing-of-gait in P1. We evaluated the impact of the spinal cord neuroprosthesis and DBS therapies on freezing-of-gait by having a trained neurologist observe the videos of each of the freezing circuit trails and label freezing-of-gait epochs with 100 ms resolution. We then calculated the fraction of the time P1 spent traversing the circuit that he spent under a freezing-of-gait epoch.
Blinding. No statistical methods were used to predetermine sample size. The experimental sessions were not randomized. Yet, different trials during the NHP experimental sessions and trial sets during the P1 sessions were randomly interleaved. The investigators were not blinded to allocation during experiments and outcome assessment. Experienced technicians working at the NHP facility and not part of the study were blinded during their assessments of PD scores. They were unaware of the MPTP administration protocol or any of the details related to our experiments. We performed all data analyses, except for the semi-automatic kinematic reconstruction in the Simi Motion software, Vicon software and marking of gait events from video recordings, using automatic computer routines.
Statistical procedures. All the computed parameters were quantified and compared within each animal/patient. All data are reported as mean values and standard error of the mean (sem). Significance was analysed using the non-parametric Wilcoxon rank sum and signed-rank tests, student's t-test, bootstrapping or a Monte Carlo approach, as indicated for each test.

Author Contributions

T.M., E.M.M., N.M., C.M., F.R., S.S., M.G.P., R.J.D., A.B., G.S., C.H., N.H., L.A., D.B., F.B., M.C., P.A.S., T.D., D.W., S.P.L. technological framework. M.G.P., C.YL., L.H., D.B., Q.L., E.B., D.W., J.B., G.C., surgeries. T.M., E.M.M., N.M., C.M., F.R., S.S., M.G.P., C.V., R.J.D., A.B., L.N.B-F., Y.J., C.H., D.B., J.L., I.V., S.B., F.B., M.G., C.YL., L.H., L.P., M.Y., F.B., M.C., D.D.W., J.B., G.C. performed experiments. T.M., E.M.M., N.M., C.M., F.R., S.S., M.G.P., R.J.D., A.B., A.G., S.D.H-C., G.D., J.R., C.G.LG-M., J.S.Q., J-B.M., G.C., J.L. data analysis. Y.J., C.YL., L.H., Q.L., F.B., M.G., M.C.J., J.F.B., P.A.S., D.G. neurological evaluations. T.M., E.M.M., N.M., C.M., F.R., S.S., M.G.P., R.J.D., G.S., A.G., J.R. generated figures. A.W., H.L., S.B., W.K.D.K., Q.L., C.Q., J.B., E.B., G.C. regulatory affairs. T.M., E.M.M., F.R., R.D., L.A., D.B., W.K.D.K., Q.L., M.C., P.A.S., T.D., D.G., A.I., D.D.W., S.P.L., S.M., C.Q., J.B., E.B., G.C., conception and supervision. G.C. wrote the paper with T.M., E.M.M., F.R., M.G.P., G.S., J.B., E.B.

Competing interests

The authors declare following competing financial interests: G.C., J.B., R.D., S.M., S.L., T.M., E.M.M., and M.C. hold various patents or applications in relation to the present work. G.C. and J.B. are consultants for ONWARD medical. G.C., J.B., S.M., S.L., H.L. are founders and minority shareholders of ONWARD, a company with potential commercial interest in the presented work.

Extended data

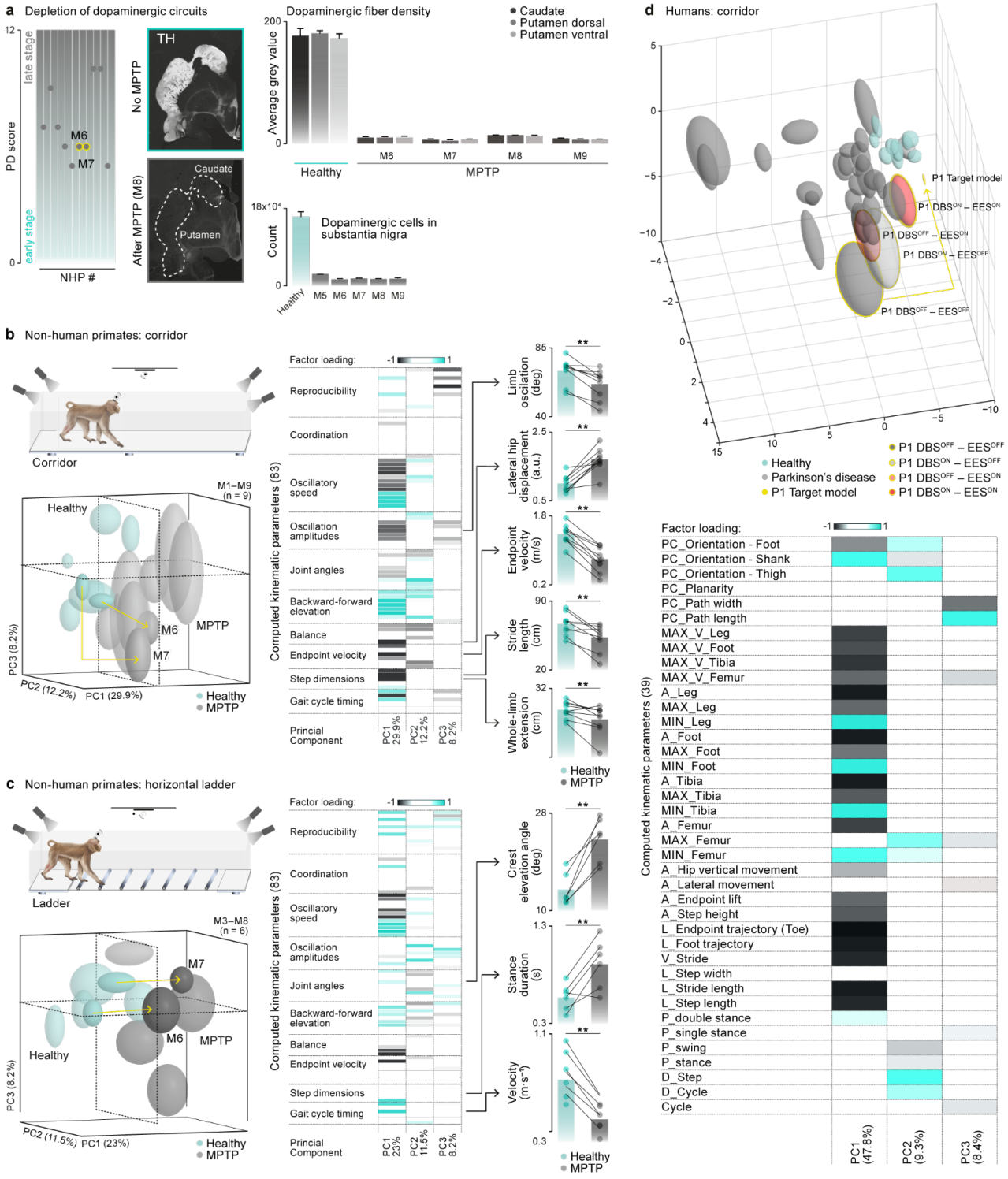

Extended data Fig. 1 | Objective quantification of gait impairments and balance problems in the NHP MPTP model of Parkinson's disease and in people with PD. a, Scatter plot shows the rounded mean of PD scores for each monkey across sessions recorded after MPTP administration. Photographs show the dopaminergic projections labelled with tyrosine hydroxylase (TH) in the putamen and caudate of a healthy monkey and in M8. The bar plots show the density of TH-labelled projections in the putamen and caudate and count of dopaminergic cells in substantia nigra in healthy controls (Ctr, n = 3) and each of the monkeys involved in MI recordings. **b-c,** The NHPs were trained to walk across a 3m-long

corridor (M1-9, n = 9) and along the rungs of a 3m-long horizontal ladder (M3-8, n = 6). Both runways were embedded within Plexiglass enclosures that allowed the NHPs to behave freely and untethered while anatomical landmarks painted on the joints were filmed using 4 or 6 cameras in order to reconstruct whole-body kinematics in 3D. We used these kinematic recordings to compute 83 variables from each gait cycle that quantified kinematic features of monkeys' locomotor patterns (**Supplementary Table 3**). This dataset was arranged in a matrix with variables as the matrix columns and each row representing one gait cycle. Data collected from different conditions (before and after MPTP administration) and different monkeys were pooled together in a single matrix and z-scored across columns. Two different tasks, corridor (a) and ladder (b), were analysed separately. We then applied PCA on this dataset and visualized the outcome by plotting the dataset in a new space spanned by the three leading PCs. The data for each monkey and condition is represented by a balloons – ellipsoids with the centre and principal semi-axis as the mean and standard deviation calculated across all the gait cycles for that condition and monkey (number of gait cycles in corridor: before MPTP: M1: 4, M2: 6, M3: 18, M4: 13, M5: 14, M6: 22, M7: 14, M8: 95, M9: 49; after MPTP: M1: 28, M2: 8, M3: 16, M4: 22, M5: 11, M6: 6, M7:9, M8: 48, M9: 59; ladder: before MPTP: M3: 12, M4: 25, M5: 23, M6: 19, M7: 9, M8: 40; after MPTP: M3: 18, M4: 7, M5: 24, M6: 31, M7: 24, M8: 14). Since the variance in the dataset is driven by the changes in gait parameters between the healthy and MPTP conditions consistent across monkeys, the parameters that best capture gait and balance deficits after MPTP administration have the highest loading factors in leading principal components (PCs). The colorplot shows the loading factors for the three leading PCs. The bar plots report the mean values of the parameters with the highest factor loadings. These parameters reflect gait and balance deficits commonly observed in people with PD. **d,** Healthy subjects (H; n = 9) and subjects with PD (PD; n=25) walked straight overground as we recorded their full-body kinematics in 3D using the Vicon multi-camera system. We used these kinematic recordings to compute 35 variables from each gait cycle that quantified kinematic features of human locomotor patterns (**Supplementary Table 5**). As for the monkeys, we arranged this dataset in a gait parameters x gait cycles matrix, applied PCA on this dataset and visualized the outcome by plotting the distribution balloons for each subject in a space spanned by the three leading PCs (number of gait cycles: H1: 37, H2: 36, H3: 33, H4: 44, H5:42, H6: 38, H7: 45, H8: 33, H9: 39; PD1: 28, PD2: 30, PD3: 54, PD4: 53, PD5: 81, PD6: 47, PD7: 69, PD8: 37, PD9: 8, PD10: 100, PD11: 32, PD12: 22, PD13: 48, PD14: 25, PD15: 69, PD16: 70, PD17: 33, PD18: 61, PD19: 40, PD20: 29, PD21: 82, PD22: 8, PD23: 66, PD24: 33, PD25: 29). The colorplot shows the loading factors for the three leading PCs. *, ** $p < 0.05$ and $p < 0.01$, respectively, using Wilcoxon signed rank test. Error bars, sem.

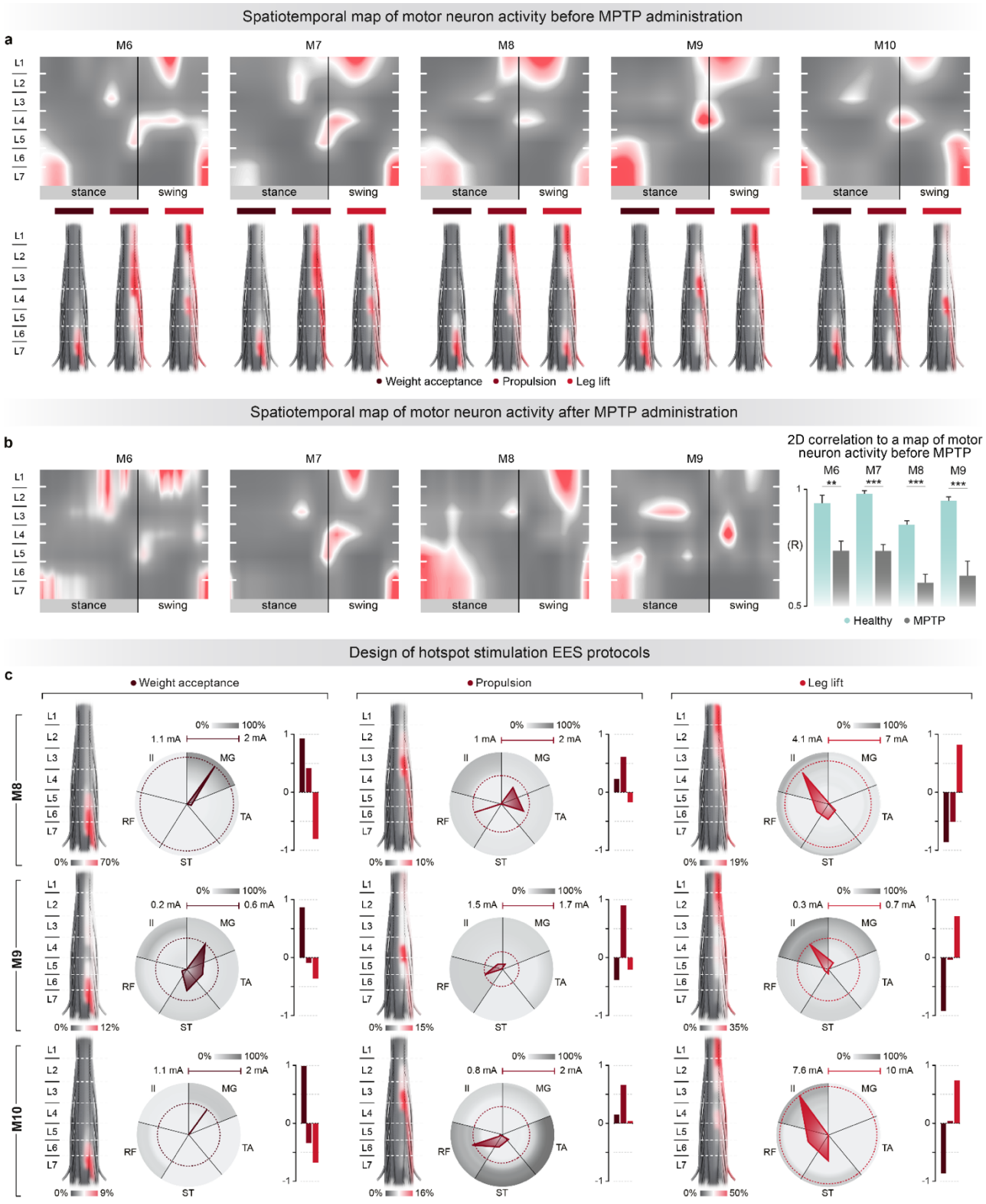

Extended data Fig. 2 | Design of EES protocols based on spatiotemporal maps of motor neuron activity. a, Colorplots showing the average spatiotemporal map of motor neuron activity underlying locomotion in M6 (n = 12 gait cycles), M7 (n = 10), M8 (n = 20), M9 (n = 32) and M10 (n = 13) before MPTP administration (Healthy). We identified the hotspots of motor neuron activity using Gaussian Mixture Modelling. The spatial maps of motor neuron activity corresponding to the time at which each hotspot reached a maximum (centre) are laid over the schematics of the spinal

cord. **b,** Colorplots show the spatiotemporal maps of motor neuron activity underlying locomotion in M6 (n = 55 gait cycles), M7 (n = 44), M8 (n = 17) and M9 (n = 11) after MPTP administration (MPTP). Bar plots compare the surface correlation between two maps calculated before MPTP administration and between a map calculated before MPTP administration and a map calculated after the MPTP administration. **c,** Circular plots reporting the amplitude (grey scale) of muscle responses recorded from leg muscles when delivering single-pulse EES at increasing amplitudes (radial axis). Red circles highlight the optimal amplitude while the polygon quantifies the muscular selectivity at this amplitude. Spatial map of motor neuron activity corresponding to optimal EES amplitudes are laid over the schematics of the spinal cord for each hotspot. Bar plots report the correlation between each maximal-selectivity spatial map of motor neuron activity and the spatial map corresponding to the targeted hotspot. Muscle responses were normalized to the maximum amplitudes observed across all the recording sessions. $p < 0.01$, $p < 0.001$, respectively, using non-parametric Monte Carlo permutation test. Error bars show sem.

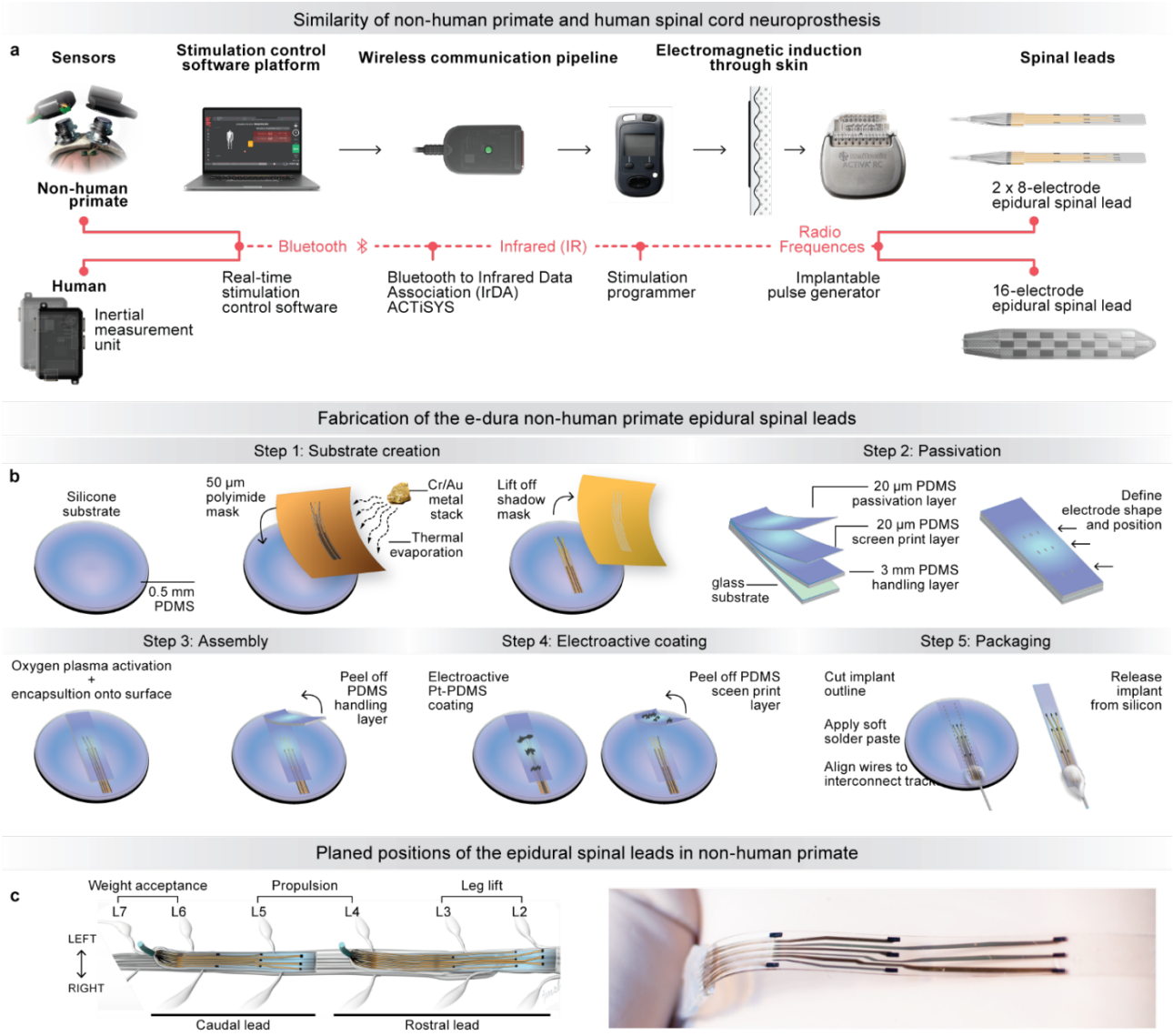

Extended data Fig. 3 | Brain-controlled spinal cord neuroprosthesis technology. a, The scheme illustrates the similarity between non-human primate and human implementation of the spinal cord neuroprosthesis. In both implementations, sensors collected physiological signals that are wirelessly acquired by the control computer running a stimulation control software. This software processed the sensor signals and used a rLDA algorithm to detect hotspot initiation events. On detection of an event, the stimulation control software sent a command to the implanted pulse generator via a wireless communication pipeline that featured electromagnetic induction though the users' skin. On reception of the command, the implanted pulse generator modified the EES sequence to promote the activity of the detected hotspot and, therefore, reinforce the intended movements. Modified EES was delivered over the posterior spinal cord by the epidural spinal leads. Between non-human primate and human implementations, only the sensors and the spinal leads differed. Non-human primate implementation relied on recordings from neurosensors featuring microelectrode arrays implanted into the leg area of the motor cortex; and on custom spinal leads designed for Rhesus macaque spinal anatomy. Human implementation relied on recordings from wearable non-invasive IMU sensors distributed across major anatomical landmarks; and on clinically-approved epidural spinal leads. The remainder of the spinal cord neuroprosthesis implementation was identical. **b,** We developed a fabrication process to manufacture the non-human primate epidural spinal leads used in M11 using *e-dura* technology (see Methods). **Step 1:** Substrate creation. We used 4" silicon wafers as substrate to prepare the leads. (top) A polystyrene sulfonic acid layer is spin coated on the carrier to provide a water-release layer for the substrate stack. A PDMS layer is subsequently cast on the substrate until reaching a thickness of approximately 500 µm. (middle) A laser-machined, 50 µm thick polyimide mask is then manually laminated on the PDMS surface, and the carriers are then mounted in a thermal evaporation chamber. A stack of chromium and gold is thermally

evaporated on the carriers through the polyimide masks, at a thickness of 5 nm (Cr) and 55 nm (Au). The chromium acts as adhesion promoter for the gold interconnect on PDMS. (bottom) The polyimide shadow mask is then peeled off the surface, revealing the interconnect design patterned in the metal stack. **Step 2**: Passivation. (top) A 3 mm thick PDMS handling layer is cast in a Petri dish. Once cured, the top surface is exposed to an oxygen plasma and a vapour-phase 1H,1H,2H,2H-perfluorooctyltriethoxysilane layer is applied in a vacuum chamber. This process inhibits the adhesion of the silicone to subsequent PDMS layers deposited on the surface. Two subsequent 20 µm thick PDMS layers are spin-coated and cured on the thick PDMS, separated by the same adhesion inhibiting layer. A slab of this triple PDMS stack (3 mm, 20 µm, 20 µm in cross section) is then cut with a blade and mounted on a glass slide. (bottom) A mechanical catheter puncher is used to make holes through the two thin PDMS layers and into the thick handling layer, in order to machine the passivation stack with through-vias. Each via is created by punching a series of 4 round holes of 690 µm diameter with 400 µm centre-to-centre spacing. **Step 3:** Assembly. (top) The top surfaces of the substrate and triple stack encapsulation are exposed to oxygen plasma, then mounted on an alignment rack, with the two treated surfaces facing one another. The vias machined in the encapsulation are aligned with the interconnect patterned on the substrate, and the two parts are then put into contact in order to form a covalent bond between the silicone layers. (bottom) Once bonded, the thick PDMS handling layer is peeled off the substrate, leaving the interconnect encapsulated by two 20 µm thick PDMS layers with openings corresponding to the position of the electrodes. **Step 4:** Electroactive coating. (top) The electroactive coating is prepared as a composite material obtained by dispersing microscale platinum particles (3.5 µm maximum particle size) within a polydimethylsiloxane (PDMS) matrix. This creates a conductive paste that offers a balance between the charge injection properties of platinum and the mechanical properties of PDMS. The composite paste is applied on the encapsulation through the screen print PDMS layer, filling the openings to make an electrical contact with the interconnect. (bottom) The screen print layer is then peeled off to remove the excess coating and define the active stimulation sites. **Step 5:** Packaging. (top) The assembled implant is manually cut while still on wafer to the desired shape using a blade. Electrical wires are threaded in a PDMS guiding piece through holes that are machined at the same pitch as the gold tracks on the substrate. This soft connector is aligned and placed onto the interconnect with wires close to the ends of the gold tracks. Conductive Silver paste is then pressure dispensed to form individual electrical connections between the wires and the gold tracks. Once all electrical connections are made, a bolus of room temperature vulcanisation sealant (one component silicone sealant 734, Dow Corning) is applied over the connector to mechanically secure the assembly. (bottom) After the sealant is cured, the implant is released from the silicon carrier by dissolving the PSS layer under the PDMS substrate with DI water. All silicone layers are prepared by mixing polydimethylsiloxane using a weight ratio of 10:1 between pre-polymer and cross-linker. The deposited layers are cured for a minimum of 3 hours in a temperature-controlled oven set to 80°C. Photographs show a fabricated *e-dura* spinal implant, including a zoom on the electrode contacts. **c,** We exploited our fabrication process to produce epidural spinal leads that embedded laterally-located electrodes targeting the left and right posterior roots of the lumbar spinal cord, as well as midline-located electrodes targeting the ascending fibres within the dorsal column. The spinal cord was reconstructed from a magnetic resonance imaging scan of a rhesus macaque onto which we represented the planed locations of the rostral and caudal spinal leads.

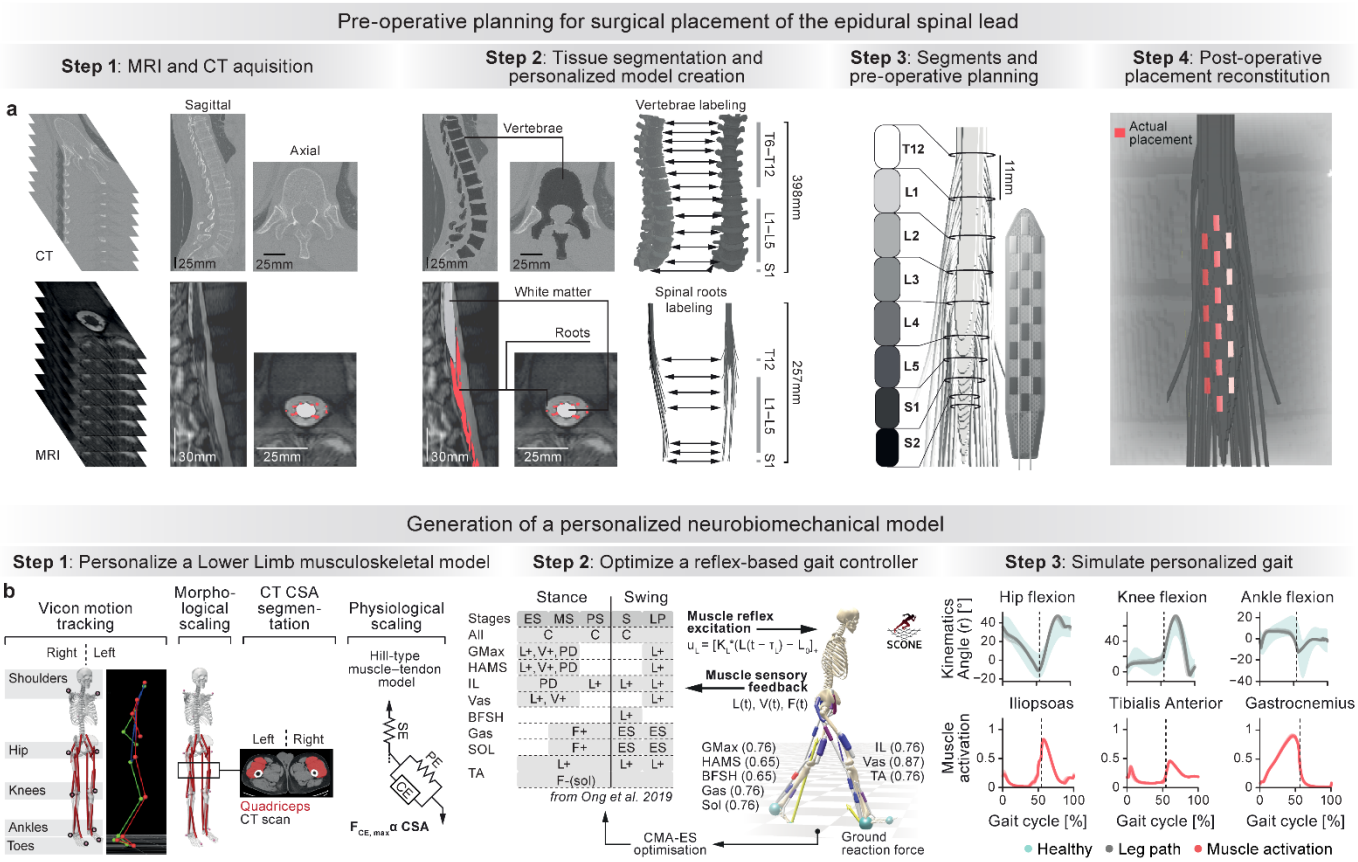

Muscles abbreviations | **BFSH**: Biceps Femoris Short Head, **Gas**: Gastrocnemius, **GMax**: Gluteus Maximus, **HAMS**: Hamstring muscles, **IL**: Iliopsoas, **Sol**: Soleus, **TA**: Tibialis Anterior, **Vas**: Vasti
Gait cylces stages | **ES**: Early Stance, **MS**: Mid-Stance, **PS**: Pre-Swing, **S**: Swing, **LP**: Landing Preparation
Low level control laws | **C**: Constant signal, **L**: muscle Length, **V**: muscle Velocity, **PD**: Proportional-Derivative control, **F**: muscle Force, **±**: positive and negative feedback

Extended data Fig. 4 | Procedures to achieve spinal cord neuroprosthesis in human. a. We used the P1's CT and MRI scans to generate a three-dimensional anatomical model of the spine, which we then used to plan the surgical placement of the epidural spinal lead over the entire lumbar spinal cord. **Step1**: P1 underwent a CT and a structural 1.5T MRI scan of his spine. **Step 2:** We segmented the vertebral bones and disks from the CT scan, and segmented the spinal cord tissues (spinal cord, spinal cord roots and cerebrospinal fluid) from the MRI scan. We co-registered the tissues segmented from the two different scans, and combined them into a 3D anatomical model of the P1 spine. **Step 3:** We loaded a 3D model of the spinal lead and placed it centred over the dorsal side of the spinal cord covering the L1-L5 spinal segments. Position of the lead with respect to the segmented vertebral column determined the insertion point of the lead to be between L1 and T12 vertebra. During the surgery, we opened the access to the surface of the dura by small incisions and a T12/L1 flavectomy, placed the tip of the lead over the midline of the exposed dura and advanced the lead rostrally to the target location. We accurately adjusted the medial and segmental position of the paddle lead by monitoring the muscle responses to single-pulse EES delivered by different lead electrodes**. Step 4:** After the surgery, we performed a post-operative CT scan to reconstruct the position of the spinal lead with respect to the patient spine. The actual placement of the lead was within 1cm of the preoperative plan, as expected due to segmentation and co-registration inaccuracies. **b,** In order to estimate the target for the immediate effects of our therapy, we sought to simulate the gait of P1 given his anatomy but in the absence of neurodegeneration. To this end, we generated a personalized neurobiomechanical model of P1. **Step1:** We personalized the Lower Limb model[78] to P1's anatomy using morphological and physiological scaling. We performed the morphological scaling based on full-body motion tracking using the Vicon system. We then implemented the physiological scaling based on segmentation of muscles' cross-sectional area (CSA) from CT images. **Step2:** We optimized the reflex-based gait controller using the SCONE software[79,87]. This controller is composed of phase dependent reflexes providing muscle excitation based on muscle length, velocity or force feedback. **Step3:** We simulated P1 gait in the absence of neurodegeneration using Covariance Matrix Adaptation Evolutionary Strategy (CMA-ES)[88] to optimize controller parameters. About 500 generations of CMA-ES were necessary to reach a stable gait from initialization. Once the parameters of the controller have converged, we generated 200 steps of this model and extracted full kinematics of lower limbs and muscle activity.

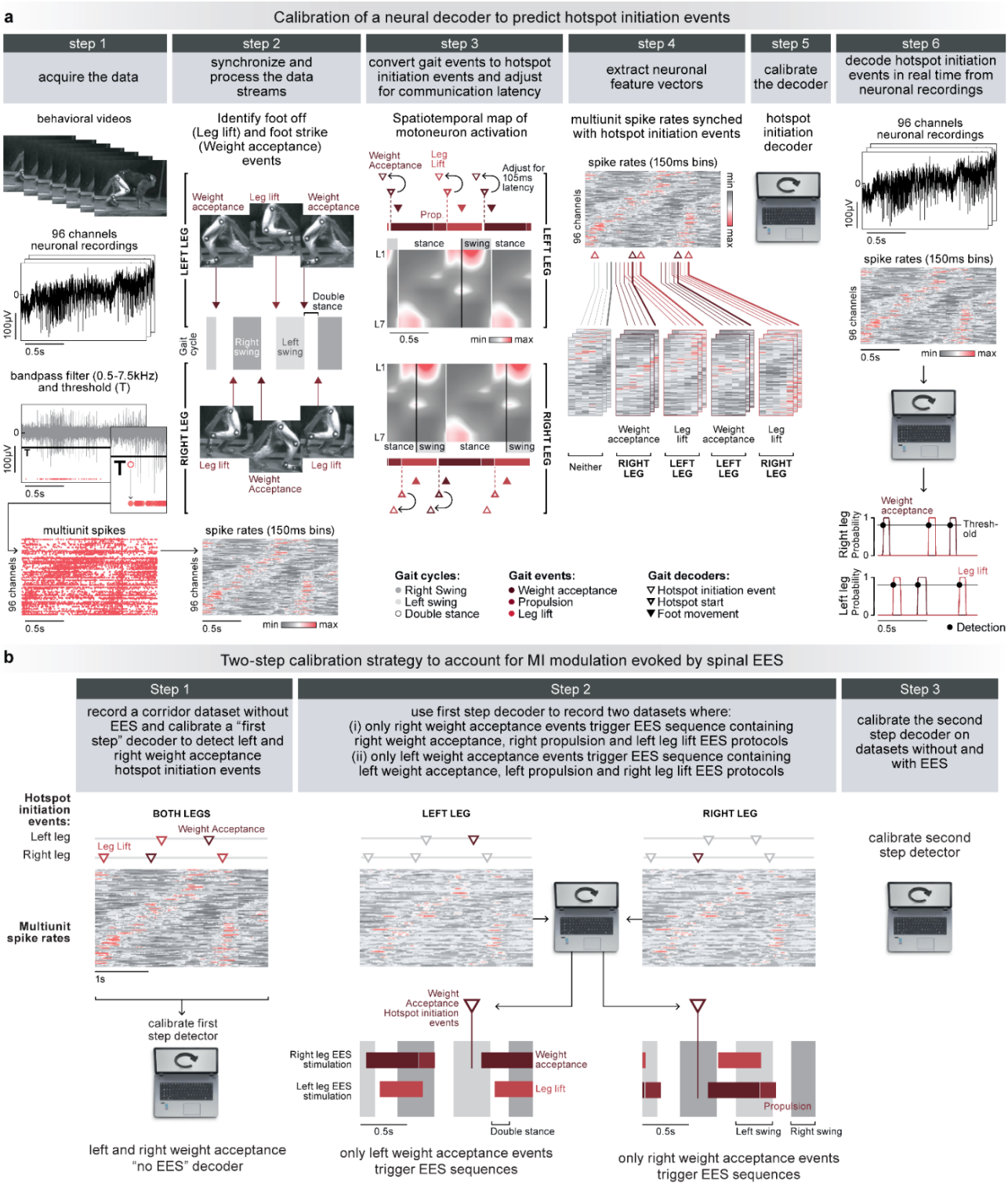

Extended data Fig. 5 | Calibration of neural decoders for real-time detection of hotspot initiation events. a. Step 1: Hindlimb kinematics and MI activity were recorded during locomotion. The neural signals were band-pass filtered (0.5-7.5kHz), and multiunit spike events were collected based on a threshold set at 3.5 times the standard deviation. **Step 2:** We marked video frames containing left and right foot off and foot strike events. We estimated multiunit spike rates from overlapping 150 ms bins that were updated every 0.5 ms. **Step 3:** We identified the right weight acceptance and right leg lift hotspots initiation events from the spatiotemporal map of motor neuron activity by aligning the gait events to the derived

map of spatiotemporal motor neuron activity. The left hotspot initiation events were derived using the same process, assuming symmetry between both legs. The hotspot events were adjusted to account for the stimulation latency of 105 ms. **Step 4:** We extracted feature vectors that originated at hotspot events and assigned them to respective hotspot classes. We assigned all other feature vectors to the “neither” class. **Step 5:** We used these feature vector classes to calibrate a regularized linear discriminant analysis decoder. **Step 6:** The decoder was uploaded into our real-time analysis software application running on the control computer. Neural data was collected in real-time, processed into multiunit spike rates, and passed through the decoder that calculated the probabilities of hotspot events. When one of the hotspot event probabilities crossed a threshold of 0.8, a wireless command was sent to the implanted pulse generator to trigger the respective stimulation sequences. These sequences were composed of one or more stimulation protocols, each designed to reinforce one of six hotspots: left and right weight acceptance, propulsion and leg lift hotspots. **b.** Two-step decoder calibration. **Step 1:** Data are acquired without EES to calibrate the first-step decoder as shown in a. **Step 2:** An additional set of data is acquired during which the first step decoder trigger composite stimulation sequences once per gait cycle. This sparse triggering mitigates the ability of EES to influence the neural activity used to detect the hotspot events that trigger EES. The composite EES sequences contain either left weight acceptance, left propulsion and right leg lift; or right weight acceptance, right propulsion and left leg lift EES protocols. **Step 3:** A second step decoder is then calibrated using all the acquired datasets. Since the decoder is calibrated on neural activity that is non-affected and affected by EES, the decoder maintains high accuracy regardless of the presence or absence of EES.

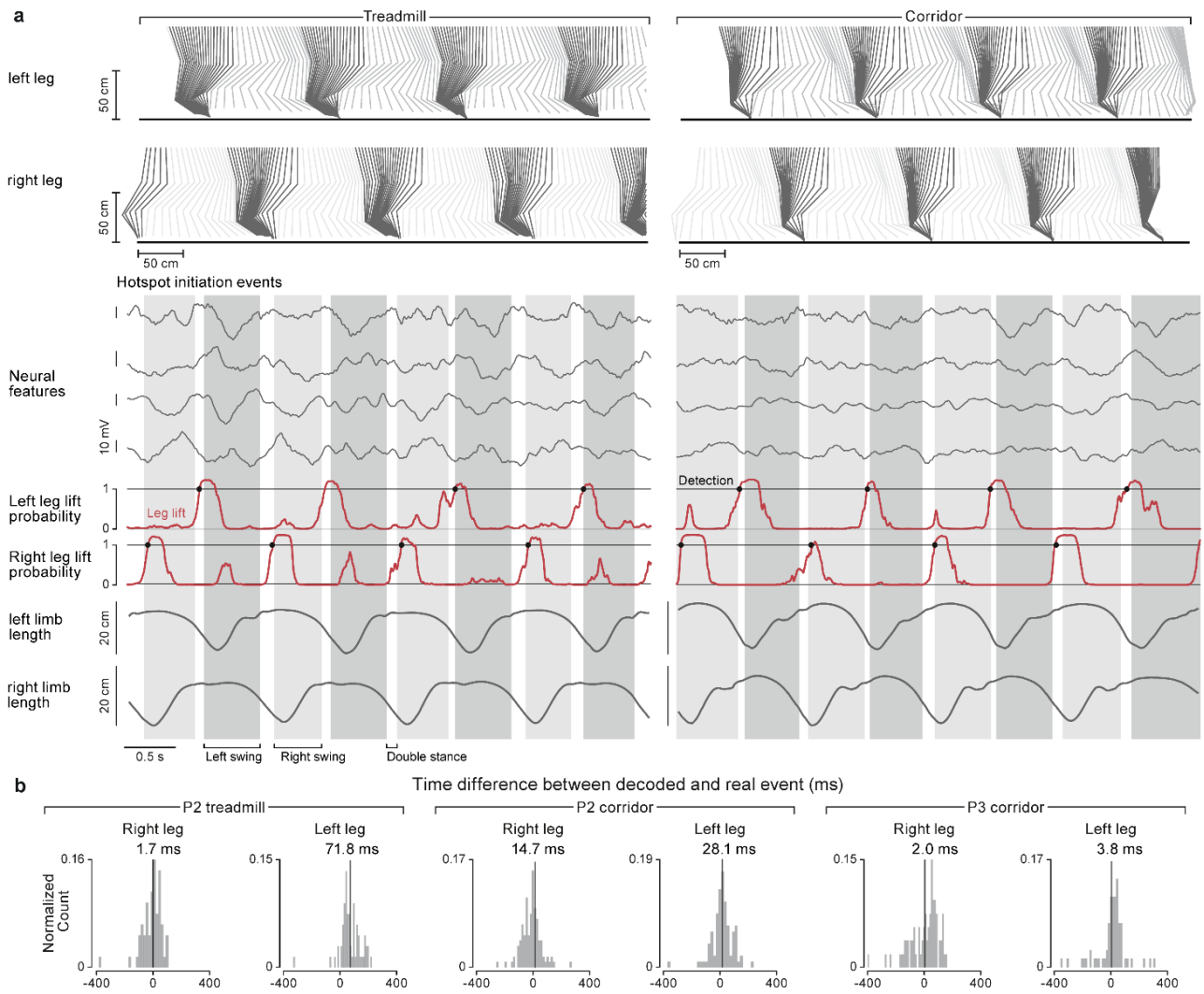

Extended data Fig. 6 | ECoG signals collected from the surface of the motor cortex of people with Parkinson's disease enable accurate detection of hotspot initiation events during locomotion. a, Examples of locomotor execution along the treadmill (5s) and corridor (5s) of participant P2. From top to bottom: stick diagram decompositions of left and right leg movements; neural features (low-pass filtered ECoG signal) from all four recorded channels; probability of left and right weight acceptance events with detected hotspot events (black dots); left and right limb length calculated as distance from the hip to the ankle joint. The white, light grey and dark grey backgrounds correspond to double stance, left and right swing gait phases, respectively. **b,** Decoding remains accurate for both tasks in P2 and for P3. Histogram plots show the distribution of the temporal differences between real and detected events (events: P1 treadmill: left: 92; right: 118; P1 corridor: left: 64; right: 62; P2 corridor: left: 70; right: 74) calculated by offline analysis using cross-validation. Median temporal difference is provided and marked by a vertical blue line.

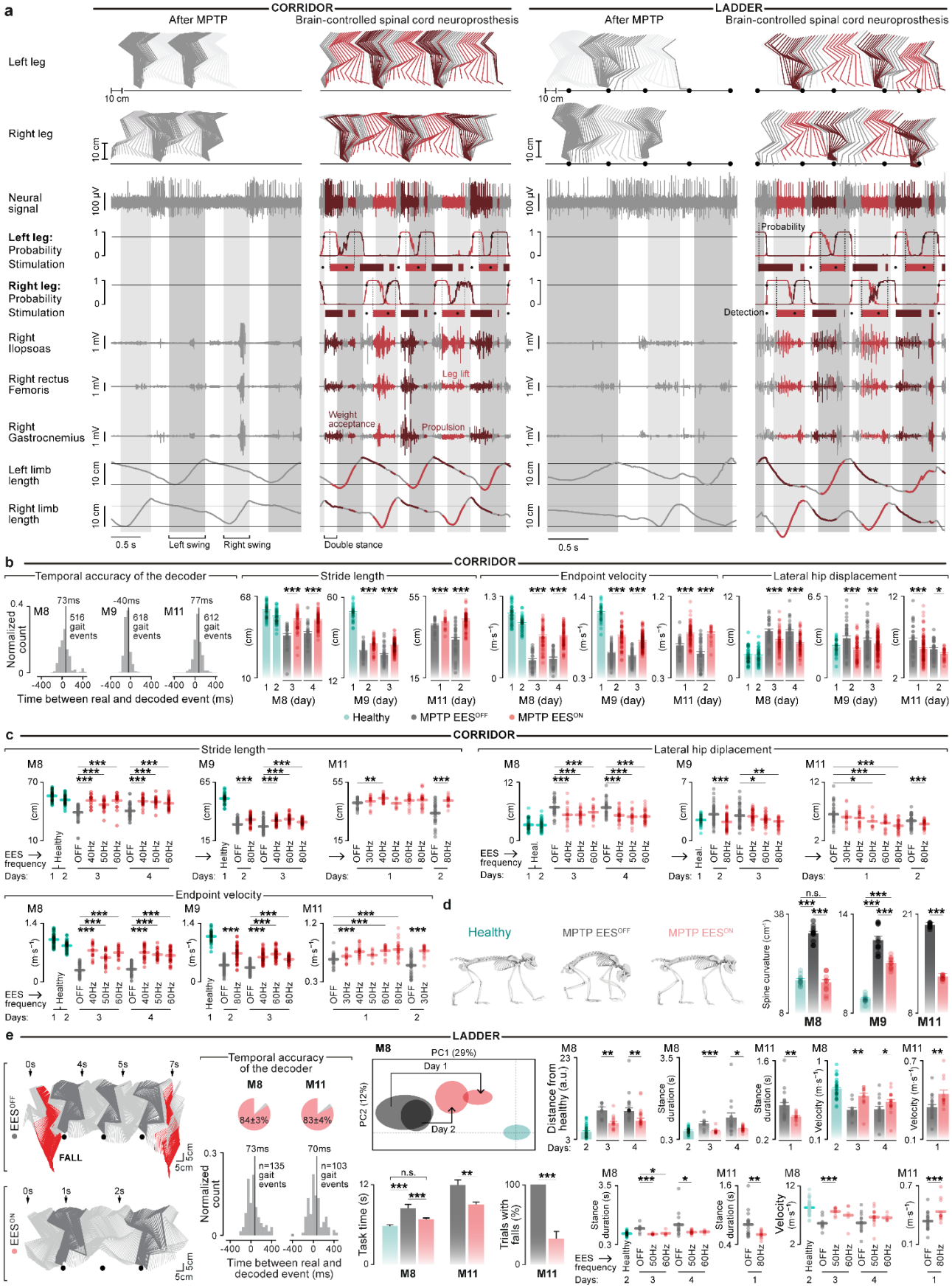
a
CORRIDOR
After MPTP
Brain-controlled spinal cord neuroprosthesis
LADDER
After MPTP
Brain-controlled spinal cord neuroprosthesis
Left leg
Right leg
10 cm
Neural signal
100 µV
Left leg: Probability
Stimulation
Right leg: Probability
Stimulation
Right Iliopsoas
Right rectus Femoris
Right Gastrocnemius
1 mV
Left limb length
Right limb length
Probability
Detection
Leg lift
Weight acceptance
Propulsion
0.5 s
Left swing
Right swing
Double stance
b
CORRIDOR
Temporal accuracy of the decoder
Normalized count
M8
73ms
516 gait events
M9
-40ms
618 gait events
M11
77ms
612 gait events
Time between real and decoded event (ms)
Stride length
Endpoint velocity
Lateral hip displacement
(cm)
(m s⁻¹)
M8 (day)
M9 (day)
M11 (day)
Healthy
MPTP EES^OFF
MPTP EES^ON
c
CORRIDOR
Stride length
Lateral hip diplacement
Endpoint velocity
EES frequency
Days:
Healthy
OFF
30Hz
40Hz
50Hz
60Hz
80Hz
d
Healthy
MPTP EES^OFF
MPTP EES^ON
Spine curvature (cm⁻¹)
n.s.
e
LADDER
EES^OFF
EES^ON
FALL
5cm
Temporal accuracy of the decoder
84±3%
83±4%
73ms
70ms
n=135 gait events
n=103 gait events
Time between real and decoded event (ms)
PC1 (29%)
PC2 (12%)
Day 1
Day 2
Distance from healthy (a.u.)
Stance duration (s)
Velocity (m s⁻¹)
Task time (s)
Trials with falls (%)

Extended data Fig. 7 | The brain-controlled spinal cord neuroprosthesis improves basic and skilled locomotion after MPTP administration. a, Examples of locomotor execution along the corridor (3.3s) and ladder (2.4s) without stimulation (left columns) and when using the brain-controlled spinal cord neuroprosthesis in M8 after MPTP administration. From top to bottom: stick diagram decompositions of left and right leg movements; neural recording from a single channel; probability of left and right weight acceptance events; detected hotspot events (broken vertical lines), periods of stimulation through the electrodes targeting the left and right weight acceptance, propulsion and leg lift hotspots; electromyographic signals; whole-limb extension calculated as distance from the hip to the ankle joint. The white, light grey and dark grey backgrounds correspond to double stance, left and right swing gait phases, respectively. **b,** The histogram plots show the distributions between hotspot initiation events measured from kinematic recordings (ground truth) and hotspot initiation events decoded during locomotion with the brain-controlled spinal cord neuroprosthesis (n = 516, 618 and 612 events for M8, M9 and M11, respectively). Bar plots report key parameters associated with gait and balance deficits commonly observed in people with PD (n = 26, 51, 27, 81, 50 and 45 steps for M8, 63, 62, 45, 140 and 55 steps for M9, and 25, 87, 33 and 19 steps for M11 across conditions from left to right). M8's gait was recorded in two days before the MPTP treatment (days 1 and 2) and two days after the treatment (days 3 and 4). M9's gait was recorded in one day before the MPTP treatment (day 1) and two days after the treatment (days 2 and 3). M11's gait was recorded in two days after the treatment (days 1 and 2). The statistical significance is shown only for comparison of between the MPTP EES^{OFF} dataset and MPTP EES^{ON} datasets recorded on the same day. **c,** Changes in EES frequency between 30 and 80 Hz modulate gait parameters but has minimal impact on the efficacy of the therapy. The plots report the mean stride length, endpoint velocity and lateral hip displacement during locomotion along the corridor (n = 50, 45, 26, 16, 17, 18, 27, 26, 22 and 33 steps for M8, 55, 63, 62, 45, 58, 43 and 39 steps for M9, and 25, 11, 29, 10, 19, 26, 33 and 19 steps for M11 across conditions from left to right) under different EES frequencies with the brain-controlled spinal cord neuroprosthesis. Small circles, individual gait cycles; lines, mean across all gait cycle for each condition. Recording days and presentation of statistical significance same as in (c). **d,** Body posture reconstructed from body kinematics using a whole-body skeletal model. Bar plots show the spine curvature measured from these reconstructions. **e,** Brain-controlled spinal cord neuroprosthesis immediately improves locomotor performance when traversing a horizontal ladder. Stick diagrams show right leg kinematics during walking along the horizontal ladder of M11 after MPTP administration without and with brain-controlled spinal cord neuroprosthesis. Pie charts report the temporal accuracy of the decoder (n = 135 and 103 events for M8 and M11 respectively) measured during the online use of the neuroprosthesis. The histogram plots show the distributions between hotspot initiation events measured from kinematic recordings (ground truth) and hotspot initiation events decoded during locomotion with the brain-controlled spinal cord neuroprosthesis (n = 135 and 103 events for ladder for M8 and M11, respectively). Bar plots repot "task" time needed to complete the task (n = 9, 30, 11 trials for M8 and 6, 14 trials for M11 across conditions from left to right) and the occurrence of falls (n = 30 trials). Balloons show mean ± standard deviation of all gait cycles for a given condition in space defined by PC1 and PC2, which explained 41% of all the variance. Bar plots report the Euclidean distance in the full 83-dimensional space of gait parameters between each gait cycle and the mean values across all the gait cycles recorded during two independent sessions before MPTP administration; as well as key parameters associated with gait and balance deficits commonly observed in people with PD (Ladder: n = 10, 13, 14, 19 and 40 steps for M8, and 20 and 12 steps for M11 across conditions from left to right). Changes in EES frequency between 30 and 80 Hz modulates gait parameters but has minimal impact on the efficacy of the therapy in the ladder. The plots report the stance duration and velocity during locomotion along the ladder (n = 40, 10, 8, 5, 14, 14 and 5 steps for M8, and 20 and 12 steps for M11 across conditions from left to right) under different EES frequencies with the brain-controlled spinal cord neuroprosthesis. Small circles, individual gait cycles; thick lines, mean across all gait cycle for each condition. Recording days and presentation of statistical significance same as in (c). *,**,*** significant difference at $p < 0.05$, $p < 0.01$ and $p < 0.001$, respectively using Wilcoxon rank sum test or the Monte Carlo permutation test. Error bars show sem.

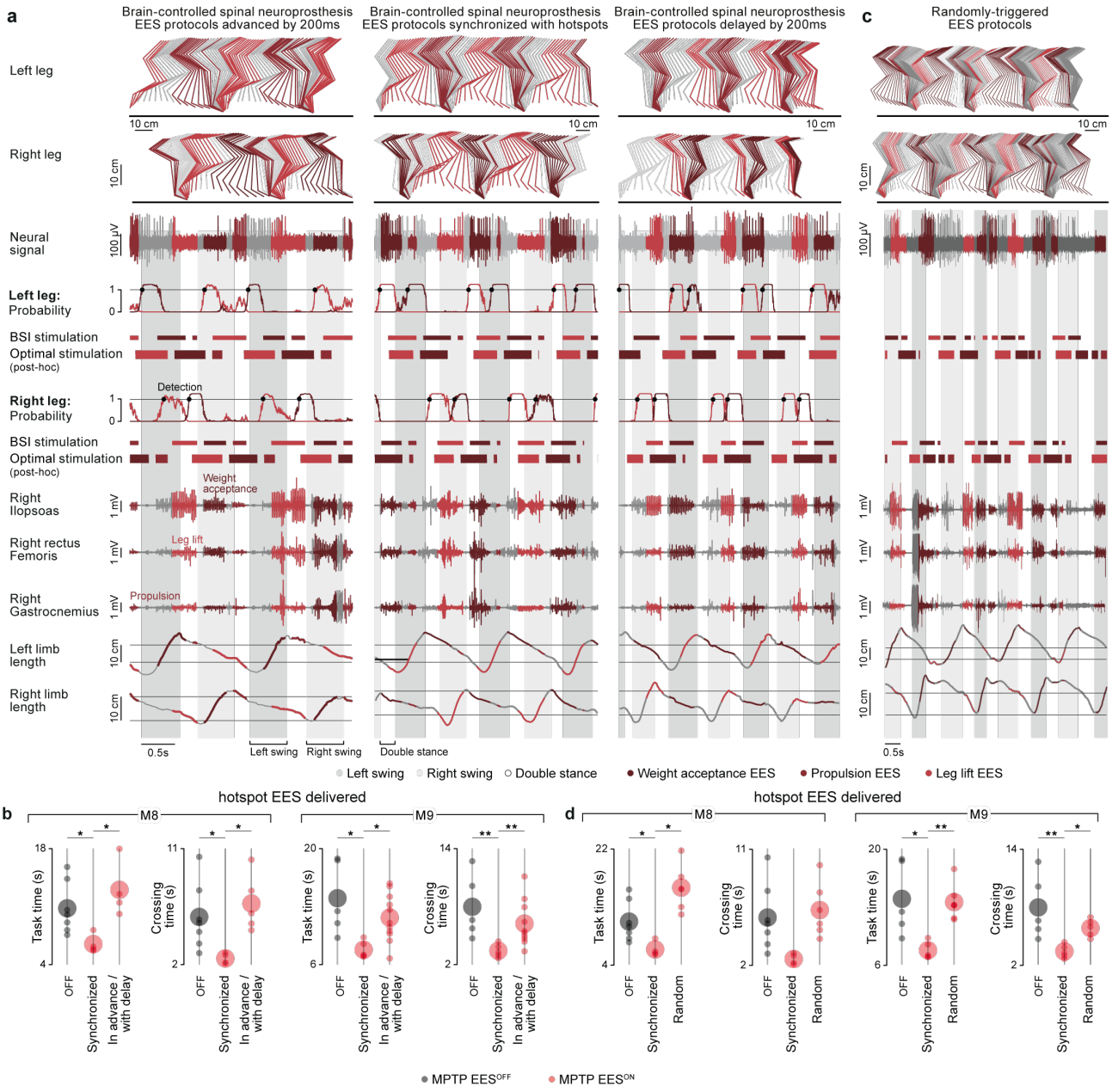

Extended data Fig. 8 | EES protocols must be synchronized precisely with hotspot initiation events for maximum efficacy of the brain-controlled spinal cord neuroprosthesis. a, Examples showing 3.3s of locomotion across the corridor using the brain-controlled spinal cord neuroprosthesis with three different decoding models (M8). From left to right: hotspot stimulation protocols initiated 200 ms before their initiation, hotspot stimulation protocols synchronized with hotspot initiation, hotspot stimulation protocols initiated 200 ms after their initiation. Conventions are the same as in **Extended Data Fig. 7a. b,** Dot plots showing the task time and crossing time without stimulation and when using the brain-controlled spinal cord neuroprosthesis delivering synchronized, advanced or delayed EES (task time: n = 7, 4 and 4 trials for M8 and 5, 5 and 11 trials for M9; crossing time: n = 7, 4 and 5 trials for M8 and 5, 5 and 11 trials for M9 for conditions from left to right, respectively). c, Example showing 7.16s of locomotion across the corridor during the randomly triggered stimulation protocols. Conventions are the same as in Extended Data Figure 7a. d, Dot plots showing the task time and crossing time without stimulation, when using the brain-controlled spinal cord neuroprosthesis to deliver synchronized EES, and random delivery of EES (task time: n = 7, 4 and 5 trials for M8 and 5, 5 and 5 trials for M9; crossing time: n = 7, 4 and 5 trials for M8 and 5, 5 and 5 trials for M9 for conditions from left to right, respectively). *, ** significant difference at $p < 0.05$ and $p < 0.01$, respectively, using Wilcoxon rank sum test.

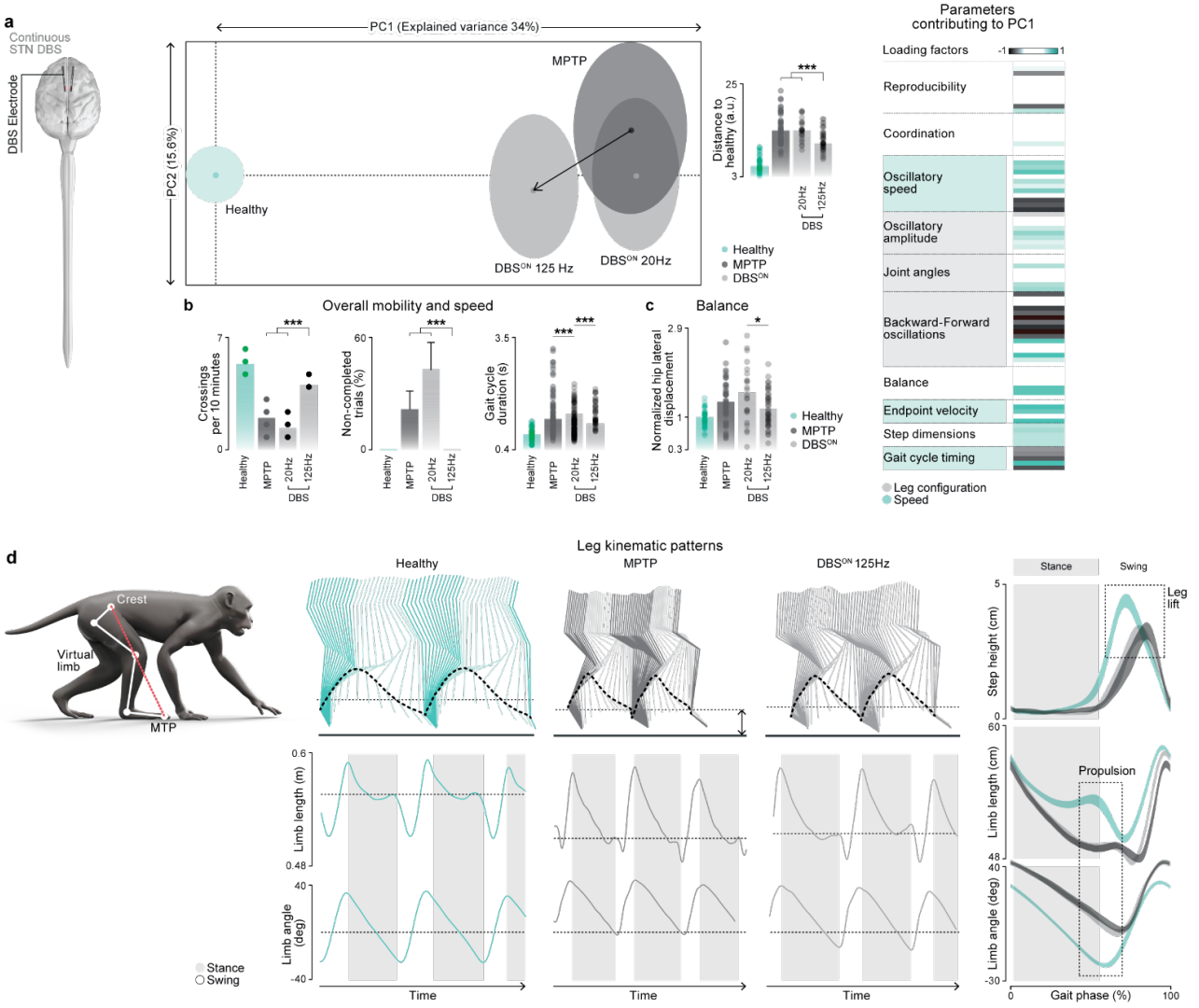

Extended data Fig. 9 | DBS reduces bradykinesia in an NHP MPTP model of PD. a, We implanted monkey M9 with mini-DBS electrodes in the left and right subthalamic nucleus after the MPTP treatment to test the effect of low frequency (20Hz) and high frequency (125Hz) DBS during corridor walking. We evaluated the locomotor performance for the following conditions: before MPTP administration (Healthy) and after MPTP administration with stimulation off (MPTP), using 20Hz DBS (DBS^{ON} 20Hz), and using 125Hz DBS (DBS^{ON} 125Hz). Balloons show mean ± SD of all gait cycles for each condition in the space spanned by two leading PCs (number of gait cycles: Healthy: 39; MPTP: 47; DBS^{ON} 20Hz: 27; DBS^{ON} 125Hz: 37). The bar plot inset reports the Euclidean distance in the full 83-dimensional gait space between each gait cycle and the mean values across all the gait cycles recorded before MPTP administration. To identify the MPTP-induced locomotor deficits affected the most by the DBS, we identified the parameters with the highest loading factors on PC1. This analysis revealed a strong influence of DBS on parameters related to gait velocity and size, but reduced impact of limb configuration values (leg lift, propulsion) during gait. **b,** As reported in Parkinson's disease patients, high frequency DBS increases the overall mobility and mediates a moderate increase on gait speed, while the low frequency DBS fails to improve locomotion and impairs awareness. The bar plots show the number of corridor crossings within 10 minutes (number of trials: Healthy: 24; MPTP: 19; DBS^{ON} 20Hz: 12; DBS^{ON} 125Hz: 17), percentage of uncompleted trials, and gait cycle duration (number of gait cycles: Healthy: 50; MPTP: 160; DBS^{ON} 20Hz: 49; DBS^{ON} 125Hz: 137). **c,** High frequency DBS moderately improves the balance locomotor deficits. The bar plot shows the mean lateral displacement of the hip during gait (number of gait cycles same as in a). **d,** DBS failed to correct for the lack of propulsion and leg lift induced by MPTP. The plots show examples of three successive gait cycles recorded before MPTP (left column), and after MPTP without using stimulation (middle column) or using 125Hz DBS (right column). The plots show mean ± SD of left leg step height, limb length and

limb angle across the gait cycle (number of gait cycles same as in a). *, **, *** reflect a significant difference at $p < 0.05$, $p < 0.01$, $p < 0.001$ respectively, using Wilcoxon ranksum test or the Monte Carlo permutation test. Error bars show sem.

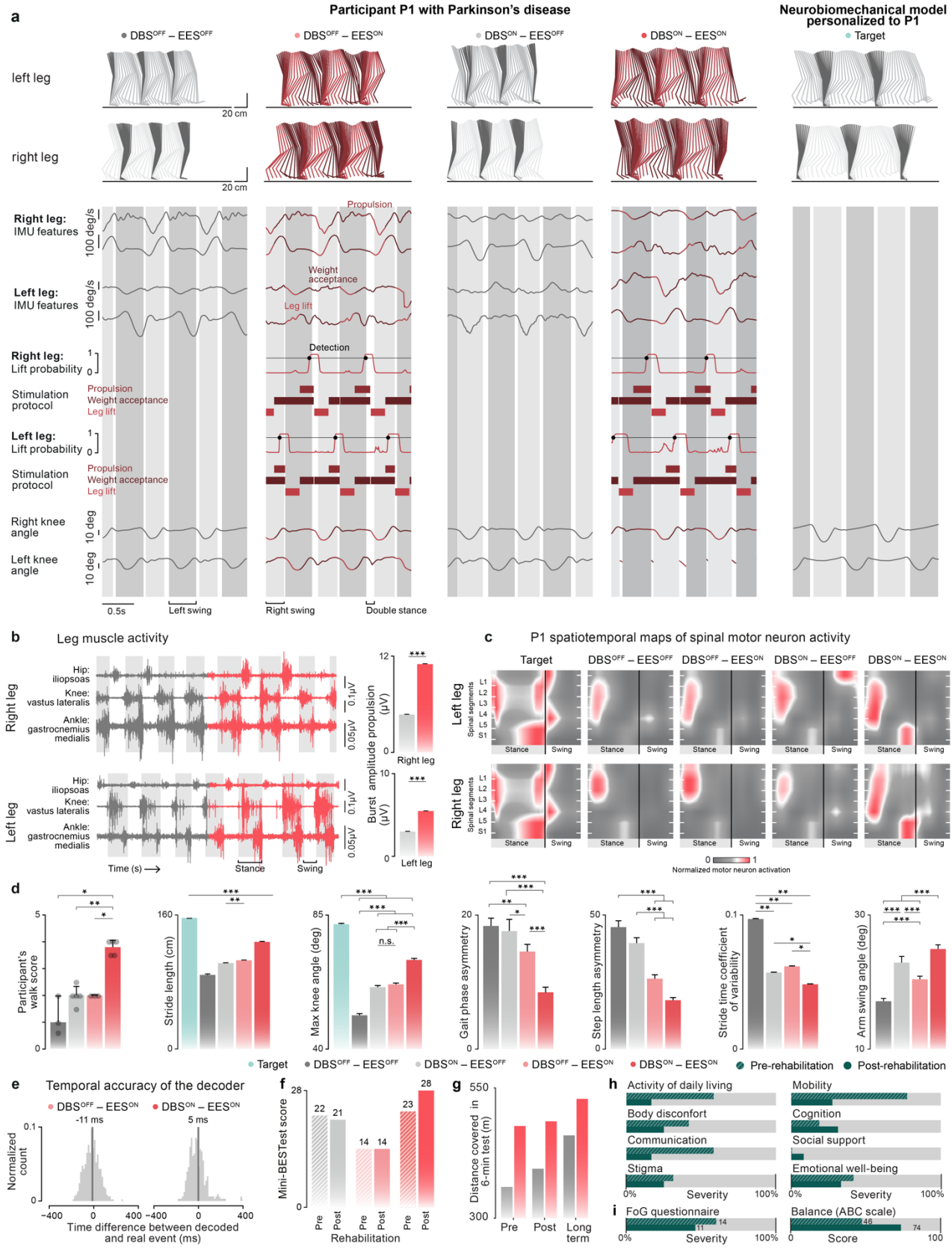

Extended data Fig. 10 | Spinal cord neuroprosthesis delivering spinal EES in synchrony with attempted

movements alleviates gait deficits of PD alone and synergistically with DBS of the subthalamic nucleus. a, Examples show 3s of P1's locomotor execution along the corridor in four combinations of using or not the kinematically-controlled spinal cord neuroprosthesis (marked "EES") and DBS of the subthalamic nucleus, and of the personalized neurobiomechanical model of P1. From top to bottom: stick diagram decompositions of left and right leg movements; four IMU features used to control the EES; probability of left and right weight acceptance events; detected hotspot events (broken vertical lines), periods of stimulation using a combination of 10 EES protocols targeting the left and right weight acceptance, propulsion and leg lift hotspots; and left and right knee angles. The white, light grey and dark grey backgrounds correspond to double stance, left swing and right swing gait phases, respectively. **b,** The plots showing EMG of left and right hip (iliopsoas), knee (gastrocnemius medialis) and ankle (vastus lateralis) leg muscles when transitioning from DBS^{ON} - EES^{OFF} into DBS^{ON} - EES^{ON} conditions illustrate the change in muscle activation. Bar plots show the burst amplitude of left and right gastrocnemius medialis muscle during the propulsion phase of gait in DBS^{ON} - EES^{OFF} (gait cycles: left: 79; right: 72) and DBS^{ON} - EES^{ON} (gait cycles: left: 136; right: 134) conditions. **c,** With the progressive use of spinal cord neuroprosthesis and DBS therapies, the motor neuron activation dynamics became more similar to that of the P1 neurobiomechanical model. The colorplots show the Target spatiotemporal spinal map derived from the P1 neurobiomechanical model, and the left and right leg spatiotemporal spinal maps of P1 in four combinations of using or not the kinematically-controlled spinal cord neuroprosthesis and DBS of the subthalamic nucleus (number of gait cycles: Target: 168; left leg: DBS^{OFF} - EES^{OFF}: 130; DBS^{ON} - EES^{OFF}: 67; DBS^{OFF} - EES^{ON}: 119; DBS^{ON} - EES^{ON}: 95; right leg: DBS^{OFF} - EES^{OFF}: 131; DBS^{ON} - EES^{OFF}: 66; DBS^{OFF} - EES^{ON}: 118; DBS^{ON} - EES^{ON}: 91). Surface correlation between the Target and therapy spatiotemporal spinal maps are shown on **Fig. 5d**. **d,** Bar plots show measures of gait quality, efficacy and symmetry, as well as balance: participants walk score (number of trials: DBS^{OFF} - EES^{OFF}: 2; DBS^{ON} - EES^{OFF}: 2; DBS^{OFF} - EES^{ON}: 5; DBS^{ON} - EES^{ON}: 5), stride length (number of gait cycles: P1 target model: 335, DBS^{OFF} - EES^{OFF}: 239; DBS^{ON} - EES^{OFF}: 120; DBS^{OFF} - EES^{ON}: 297; DBS^{ON} - EES^{ON}: 209), max knee angle (number of gait cycles: Target: 336; DBS^{OFF} - EES^{OFF}: 328; DBS^{ON} - EES^{OFF}: 175; DBS^{OFF} - EES^{ON}: 431; DBS^{ON} - EES^{ON}: 339), gait phase asymmetry (number of gait cycles: DBS^{OFF} - EES^{OFF}: 119; DBS^{ON} - EES^{OFF}: 60; DBS^{OFF} - EES^{ON}: 148; DBS^{ON} - EES^{ON}: 103), step length asymmetry as measured by the ratio between lengths of the left and right steps (number of gait cycles: P1 Target model: 167; DBS^{OFF} - EES^{OFF}: 119; DBS^{ON} - EES^{OFF}: 60; DBS^{OFF} - EES^{ON}: 148; DBS^{ON} - EES^{ON}: 103), stride time coefficient of variability (number of gait cycles same as for stride length), and arm swing angle (number of gait cycles: DBS^{OFF} - EES^{OFF}: 328; DBS^{ON} - EES^{OFF}: 175; DBS^{OFF} - EES^{ON}: 431; DBS^{ON} - EES^{ON}: 339). **e,** Decoding of hotspot initiation events from IMU signals to control the spinal cord neuroprosthesis remains accurate both when DBS is on or off. Histogram plots show the distribution of the temporal differences between real and detected events (events: DBS^{OFF} - EES^{ON}: 462; DBS^{ON} - EES^{ON}: 328) when using the brain-controlled spinal cord neuroprosthesis. Median temporal difference is provided and marked by a vertical line. **f,** The bar plots show the gains in balance, as measured using the Mini-BESTest, after the three-month rehabilitation supported by the spinal cord EES. **g,** The bar plots show improvements in endurance, as measured by the distance covered during a 6-minute walking test, after the three-month rehabilitation supported by the spinal cord EES and 1-year after. **h,** The bar plots show the sub-categories of the quality of life PDQ-39 questionnaire scores before and after the three-month rehabilitation supported by the spinal cord EES. **i,** Improvements in freezing of gait and balance, as measured by the FoG questionnaire and ABC questionnaire, prior and post-rehabilitation. *, **, *** significant difference at $p < 0.05$, $p < 0.01$, $p < 0.001$, respectively, using Wilcoxon rank sum test or the Monte Carlo permutation test. Error bars show sem.

References

1. Ge, H.L., *et al.* The prevalence of freezing of gait in Parkinson's disease and in patients with different disease durations and severities. *Chin Neurosurg J* **6**, 17 (2020).
2. Stolze, H., *et al.* Prevalence of gait disorders in hospitalized neurological patients. *Mov Disord* **20**, 89-94 (2005).
3. Fasano, A., Canning, C.G., Hausdorff, J.M., Lord, S. & Rochester, L. Falls in Parkinson's disease: A complex and evolving picture. *Mov Disord* **32**, 1524-1536 (2017).
4. Snijders, A.H., *et al.* Physiology of freezing of gait. *Annals of Neurology* **80**, 644-659 (2016).
5. Marsden, C.D. & Parkes, J.D. Success and problems of long-term levodopa therapy in Parkinson's disease. *Lancet* **1**, 345-349 (1977).
6. Funkiewiez, A., *et al.* Long term effects of bilateral subthalamic nucleus stimulation on cognitive function, mood, and behaviour in Parkinson's disease. *J Neurol Neurosur Ps* **75**, 834-839 (2004).
7. Fasano, A., Aquino, C.C., Krauss, J.K., Honey, C.R. & Bloem, B.R. Axial disability and deep brain stimulation in patients with Parkinson disease. *Nature reviews. Neurology* **11**, 98-110 (2015).
8. Collomb-Clerc, A. & Welter, M.L. Effects of deep brain stimulation on balance and gait in patients with Parkinson's disease: A systematic neurophysiological review. *Neurophysiol Clin* **45**, 371-388 (2015).
9. Fuentes, R., Petersson, P., Siesser, W.B., Caron, M.G. & Nicolelis, M.A. Spinal cord stimulation restores locomotion in animal models of Parkinson's disease. *Science* **323**, 1578-1582 (2009).
10. Santana, M.B., *et al.* Spinal cord stimulation alleviates motor deficits in a primate model of Parkinson disease. *Neuron* **84**, 716-722 (2014).
11. Pinto de Souza, C., *et al.* Spinal cord stimulation improves gait in patients with Parkinson's disease previously treated with deep brain stimulation. *Mov Disord* (2016).
12. de Lima-Pardini, A.C., *et al.* Effects of spinal cord stimulation on postural control in Parkinson's disease patients with freezing of gait. *Elife* **7**(2018).
13. Nishioka, K. & Nakajima, M. Beneficial Therapeutic Effects of Spinal Cord Stimulation in Advanced Cases of Parkinson's Disease With Intractable Chronic Pain: A Case Series. *Neuromodulation* **18**, 751-753 (2015).
14. Opova, K., Limousin, P. & Akram, H. Spinal Cord Stimulation for Gait Disorders in Parkinson's Disease. *J Parkinson Dis* **13**, 57-70 (2023).
15. de Andrade, E.M., *et al.* Spinal cord stimulation for Parkinson's disease: a systematic review. *Neurosurg Rev* **39**, 27-35; discussion 35 (2016).
16. Fuentes, R., Petersson, P. & Nicolelis, M.A. Restoration of locomotive function in Parkinson's disease by spinal cord stimulation: mechanistic approach. *Eur J Neurosci* **32**, 1100-1108 (2010).
17. Thevathasan, W., *et al.* Spinal cord stimulation failed to relieve akinesia or restore locomotion in Parkinson disease. *Neurology* **74**, 1325-1327 (2010).
18. Hassan, S., Amer, S., Alwaki, A. & Elborno, A. A patient with Parkinson's disease benefits from spinal cord stimulation. *J Clin Neurosci* **20**, 1155-1156 (2013).
19. Prasad, S., *et al.* Spinal Cord Stimulation for Very Advanced Parkinson's Disease: A 1-Year Prospective Trial. *Movement Disord* **35**, 1082-1083 (2020).
20. Capogrosso, M., *et al.* A computational model for epidural electrical stimulation of spinal sensorimotor circuits. *J Neurosci* **33**, 19326-19340 (2013).
21. Moraud, E.M., *et al.* Mechanisms Underlying the Neuromodulation of Spinal Circuits for Correcting Gait and Balance Deficits after Spinal Cord Injury. *Neuron* **89**, 814-828 (2016).

22. Wenger, N.*, et al.* Spatiotemporal neuromodulation therapies engaging muscle synergies improve motor control after spinal cord injury. *Nature medicine* **22**, 138-145 (2016).
23. Capogrosso, M.*, et al.* A brain–spine interface alleviating gait deficits after spinal cord injury in primates. *Nature* **539**, 284-288 (2016).
24. Wagner, F.B.*, et al.* Targeted neurotechnology restores walking in humans with spinal cord injury. *Nature* **563**, 65-71 (2018).
25. Rowald, A.*, et al.* Activity-dependent spinal cord neuromodulation rapidly restores trunk and leg motor functions after complete paralysis. *Nature medicine* **28**, 260-271 (2022).
26. Kathe, C.*, et al.* The neurons that restore walking after paralysis. *Nature* **611**, 540-547 (2022).
27. Bezard, E., Imbert, C., Deloire, X., Bioulac, B. & Gross, C.E. A chronic MPTP model reproducing the slow evolution of Parkinson's disease: evolution of motor symptoms in the monkey. *Brain Res* **766**, 107-112 (1997).
28. Yin, M.*, et al.* Wireless Neurosensor for Full-Spectrum Electrophysiology Recordings during Free Behavior. *Neuron* **84**, 1170-1182 (2014).
29. Mignardot, J.B.*, et al.* A multidirectional gravity-assist algorithm that enhances locomotor control in patients with stroke or spinal cord injury. *Science translational medicine* **9**(2017).
30. Cappellini, G., Ivanenko, Y.P., Dominici, N., Poppele, R.E. & Lacquaniti, F. Migration of motor pool activity in the spinal cord reflects body mechanics in human locomotion. *J Neurophysiol* **104**, 3064-3073 (2010).
31. Guiho, T., Baker, S.N. & Jackson, A. Epidural and transcutaneous spinal cord stimulation facilitates descending inputs to upper-limb motoneurons in monkeys. *Journal of Neural Engineering* **18**(2021).
32. Minev, I.R.*, et al.* Biomaterials. Electronic dura mater for long-term multimodal neural interfaces. *Science* **347**, 159-163 (2015).
33. Barra, B.*, et al.* Epidural electrical stimulation of the cervical dorsal roots restores voluntary upper limb control in paralyzed monkeys. *Nature Neuroscience* **25**, 924-934 (2022).
34. Lorach, H.*, et al.* Walking naturally after spinal cord injury using a brain-spine interface. *Nature* **618**, 126-133 (2023).
35. Milekovic, T.*, et al.* Stable long-term BCI-enabled communication in ALS and locked-in syndrome using LFP signals. *J Neurophysiol* **120**, 343-360 (2018).
36. Capogrosso, M.*, et al.* Configuration of electrical spinal cord stimulation through real-time processing of gait kinematics. *Nat Protoc* (2018).
37. Milekovic, T., Truccolo, W., Grun, S., Riehle, A. & Brochier, T. Local field potentials in primate motor cortex encode grasp kinetic parameters. *Neuroimage* (2015).
38. Milekovic, T.*, et al.* An online brain-machine interface using decoding of movement direction from the human electrocorticogram. *J Neural Eng* **9**, 046003 (2012).
39. Burciu, R.G. & Vaillancourt, D.E. Imaging of Motor Cortex Physiology in Parkinson's Disease. *Mov Disord* **33**, 1688-1699 (2018).
40. Yu, H., Sternad, D., Corcos, D.M. & Vaillancourt, D.E. Role of hyperactive cerebellum and motor cortex in Parkinson's disease. *Neuroimage* **35**, 222-233 (2007).
41. Sabatini, U.*, et al.* Cortical motor reorganization in akinetic patients with Parkinson's disease: a functional MRI study. *Brain* **123 (Pt 2)**, 394-403 (2000).
42. Eckert, T., Peschel, T., Heinze, H.J. & Rotte, M. Increased pre-SMA activation in early PD patients during simple self-initiated hand movements. *Journal of neurology* **253**, 199-207 (2006).
43. Catalan, M.J., Ishii, K., Honda, M., Samii, A. & Hallett, M. A PET study of sequential finger movements of varying length in patients with Parkinson's disease. *Brain* **122 (Pt 3)**, 483-495 (1999).
44. Turner, R.S., Grafton, S.T., McIntosh, A.R., DeLong, M.R. & Hoffman, J.M. The functional anatomy of parkinsonian bradykinesia. *Neuroimage* **19**, 163-179 (2003).

45. Milekovic, T., Ball, T., Schulze-Bonhage, A., Aertsen, A. & Mehring, C. Detection of Error Related Neuronal Responses Recorded by Electrocorticography in Humans during Continuous Movements. *PLoS One* **8**, e55235 (2013).
46. Gilron, R.e.*, et al.* Long-term wireless streaming of neural recordings for circuit discovery and adaptive stimulation in individuals with Parkinson's disease. *Nature biotechnology* **39**, 1078-1085 (2021).
47. Bruel, A.*, et al.* Investigation of neural and biomechanical impairments leading to pathological toe and heel gaits using neuromusculoskeletal modelling. *J Physiol* **600**, 2691-2712 (2022).
48. Prasanth, H.*, et al.* Wearable Sensor-Based Real-Time Gait Detection: A Systematic Review. *Sensors* **21**(2021).
49. The Unified Parkinson's Disease Rating Scale (UPDRS): status and recommendations. *Mov Disord* **18**, 738-750 (2003).
50. Nutt, J.G.*, et al.* Freezing of gait: moving forward on a mysterious clinical phenomenon. *Lancet Neurology* **10**, 734-744 (2011).
51. Grabli, D.*, et al.* Gait disorders in parkinsonian monkeys with pedunculopontine nucleus lesions: a tale of two systems. *J Neurosci* **33**, 11986-11993 (2013).
52. Rohani, M., Kalsi-Ryan, S., Lozano, A.M. & Fasano, A. Spinal Cord Stimulation in Primary Progressive Freezing of Gait. *Movement Disord* **32**, 1336-1337 (2017).
53. Samotus, O., Parrent, A. & Jog, M. Spinal Cord Stimulation Therapy for Gait Dysfunction in Advanced Parkinson's Disease Patients. *Movement Disord* **33**, 783-792 (2018).
54. Thenaisie, Y.*, et al.* Principles of gait encoding in the subthalamic nucleus of people with Parkinson's disease. *Science translational medicine* **14**, eabo1800 (2022).
55. Ahmed, M.R.*, et al.* Lentiviral overexpression of GRK6 alleviates L-dopa-induced dyskinesia in experimental Parkinson's disease. *Science translational medicine* **2**, 28ra28 (2010).
56. Bezard, E.*, et al.* The mGluR5 negative allosteric modulator dipraglurant reduces dyskinesia in the MPTP macaque model. *Mov Disord* **29**, 1074-1079 (2014).
57. Bezard, E.*, et al.* Attenuation of levodopa-induced dyskinesia by normalizing dopamine D3 receptor function. *Nat Med* **9**, 762-767 (2003).
58. Fasano, S.*, et al.* Inhibition of Ras-guanine nucleotide-releasing factor 1 (Ras-GRF1) signaling in the striatum reverts motor symptoms associated with L-dopa-induced dyskinesia. *Proc Natl Acad Sci U S A* **107**, 21824-21829 (2010).
59. Porras, G.*, et al.* PSD-95 expression controls l-DOPA dyskinesia through dopamine D1 receptor trafficking. *J Clin Invest* **122**, 3977-3989 (2012).
60. Shen, W.*, et al.* M4 Muscarinic Receptor Signaling Ameliorates Striatal Plasticity Deficits in Models of L-DOPA-Induced Dyskinesia. *Neuron* **88**, 762-773 (2015).
61. Urs, N.M.*, et al.* Targeting beta-arrestin2 in the treatment of L-DOPA-induced dyskinesia in Parkinson's disease. *Proc Natl Acad Sci U S A* **112**, E2517-2526 (2015).
62. Bezard, E.*, et al.* Relationship between the appearance of symptoms and the level of nigrostriatal degeneration in a progressive 1-methyl-4-phenyl-1,2,3,6-tetrahydropyridine-lesioned macaque model of Parkinson's disease. *Journal of Neuroscience* **21**, 6853-6861 (2001).
63. Bezard, E.*, et al.* Relationship between the appearance of symptoms and the level of nigrostriatal degeneration in a progressive 1-methyl-4-phenyl-1,2,3,6-tetrahydropyridine-lesioned macaque model of Parkinson's disease. *The Journal of neuroscience : the official journal of the Society for Neuroscience* **21**, 6853-6861 (2001).
64. Meissner, W.*, et al.* Time-course of nigrostriatal degeneration in a progressive MPTP-lesioned macaque model of Parkinson's disease. *Mol Neurobiol* **28**, 209-218 (2003).

65. Rosenblad, C.*, et al.* Vector-mediated l-3,4-dihydroxyphenylalanine delivery reverses motor impairments in a primate model of Parkinson's disease. *Brain : a journal of neurology* **142**, 2402-2416 (2019).
66. Courtine, G.*, et al.* Kinematic and EMG determinants in quadrupedal locomotion of a non-human primate (Rhesus). *J Neurophysiol* **93**, 3127-3145 (2005).
67. Tass, P.A.*, et al.* Coordinated reset has sustained aftereffects in Parkinsonian monkeys. *Ann Neurol* **72**, 816-820 (2012).
68. Schiavone, G.*, et al.* Soft, Implantable Bioelectronic Interfaces for Translational Research. *Adv Mater*, e1906512 (2020).
69. Baufreton, J.*, et al.* Inhaling xenon ameliorates l-dopa-induced dyskinesia in experimental parkinsonism. *Mov Disord* (2018).
70. Zampieri, C.*, et al.* The instrumented timed up and go test: potential outcome measure for disease modifying therapies in Parkinson's disease. *J Neurol Neurosurg Psychiatry* **81**, 171-176 (2010).
71. Palmerini, L., Mellone, S., Avanzolini, G., Valzania, F. & Chiari, L. Quantification of motor impairment in Parkinson's disease using an instrumented timed up and go test. *IEEE Trans Neural Syst Rehabil Eng* **21**, 664-673 (2013).
72. McLachlan, G.J. & Peel, D. *Finite mixture models*, (Wiley, New York, 2000).
73. Postuma, R.B.*, et al.* MDS clinical diagnostic criteria for Parkinson's disease. *Mov Disord* **30**, 1591-1601 (2015).
74. Stanslaski, S.*, et al.* A Chronically Implantable Neural Coprocessor for Investigating the Treatment of Neurological Disorders. *IEEE Trans Biomed Circuits Syst* **12**, 1230-1245 (2018).
75. Kremen, V.*, et al.* Integrating Brain Implants With Local and Distributed Computing Devices: A Next Generation Epilepsy Management System. *IEEE J Transl Eng Health Med* **6**, 2500112 (2018).
76. Pistohl, T., Ball, T., Schulze-Bonhage, A., Aertsen, A. & Mehring, C. Prediction of arm movement trajectories from ECoG-recordings in humans. *J Neurosci Methods* **167**, 105-114 (2008).
77. Moreau, C.*, et al.* STN-DBS frequency effects on freezing of gait in advanced Parkinson disease. *Neurology* **71**, 80-84 (2008).
78. Delp, S.L.*, et al.* An interactive graphics-based model of the lower extremity to study orthopaedic surgical procedures. *IEEE Trans Biomed Eng* **37**, 757-767 (1990).
79. Ong, C.F., Geijtenbeek, T., Hicks, J.L. & Delp, S.L. Predicting gait adaptations due to ankle plantarflexor muscle weakness and contracture using physics-based musculoskeletal simulations. *PLoS computational biology* **15**, e1006993 (2019).
80. Geyer, H. & Herr, H. A muscle-reflex model that encodes principles of legged mechanics produces human walking dynamics and muscle activities. *IEEE Trans Neural Syst Rehabil Eng* **18**, 263-273 (2010).
81. Song, S. & Geyer, H. Predictive neuromechanical simulations indicate why walking performance declines with ageing. *J Physiol* **596**, 1199-1210 (2018).
82. Thelen, D.G. Adjustment of muscle mechanics model parameters to simulate dynamic contractions in older adults. *J Biomech Eng* **125**, 70-77 (2003).
83. Seth, A.*, et al.* OpenSim: Simulating musculoskeletal dynamics and neuromuscular control to study human and animal movement. *PLoS computational biology* **14**, e1006223 (2018).
84. Häkkinen, K. & Häkkinen, A. Muscle cross-sectional area, force production and relaxation characteristics in women at different ages. *Eur J Appl Physiol Occup Physiol* **62**, 410-414 (1991).
85. Goodpaster, B.H.*, et al.* Attenuation of skeletal muscle and strength in the elderly: The Health ABC Study. *J Appl Physiol (1985)* **90**, 2157-2165 (2001).

86. Cotofana, S.*, et al.* Correlation between single-slice muscle anatomical cross-sectional area and muscle volume in thigh extensors, flexors and adductors of perimenopausal women. *Eur J Appl Physiol* **110**, 91-97 (2010).
87. Geijtenbeek, T. Scone: Open source software for predictive simulation of biological motion. *Journal of Open Source Software* **4**, 1421 (2019).
88. Hansen, N. & Kern, S. Evaluating the CMA Evolution Strategy on Multimodal Test Functions. in *Parallel Problem Solving from Nature - PPSN VIII* (eds. Yao, X.*, et al.*) 282-291 (Springer Berlin Heidelberg, Berlin, Heidelberg, 2004).
89. Wang, J.M., Hamner, S.R., Delp, S.L. & Koltun, V. Optimizing Locomotion Controllers Using Biologically-Based Actuators and Objectives. *ACM Trans Graph* **31**(2012).
90. Altini, N.*, et al.* Segmentation and Identification of Vertebrae in CT Scans Using CNN, k-Means Clustering and k-NN. *Informatics* **8**, 40 (2021).
91. Sekuboyina, A.*, et al.* VerSe: A Vertebrae labelling and segmentation benchmark for multi-detector CT images. *Medical Image Analysis* **73**, 102166 (2021).
92. Isensee, F., Jaeger, P.F., Kohl, S.A.A., Petersen, J. & Maier-Hein, K.H. nnU-Net: a self-configuring method for deep learning-based biomedical image segmentation. *Nat Methods* **18**, 203-211 (2021).
93. De Leener, B.*, et al.* SCT: Spinal Cord Toolbox, an open-source software for processing spinal cord MRI data. *Neuroimage* **145**, 24-43 (2017).
94. Patterson, K.K., Gage, W.H., Brooks, D., Black, S.E. & McIlroy, W.E. Evaluation of gait symmetry after stroke: a comparison of current methods and recommendations for standardization. *Gait & posture* **31**, 241-246 (2010).
95. Horak, F.B. & Mancini, M. Objective biomarkers of balance and gait for Parkinson's disease using body-worn sensors. *Mov Disord* **28**, 1544-1551 (2013).
96. Lord, S., Galna, B. & Rochester, L. Moving forward on gait measurement: toward a more refined approach. *Mov Disord* **28**, 1534-1543 (2013).
97. Franchignoni, F., Horak, F., Godi, M., Nardone, A. & Giordano, A. Using psychometric techniques to improve the Balance Evaluation Systems Test: the mini-BESTest. *J Rehabil Med* **42**, 323-331 (2010).
98. Dal Bello-Haas, V., Klassen, L., Sheppard, M.S. & Metcalfe, A. Psychometric Properties of Activity, Self-Efficacy, and Quality-of-Life Measures in Individuals with Parkinson Disease. *Physiother Can* **63**, 47-57 (2011).
99. Powell, L.E. & Myers, A.M. The Activities-specific Balance Confidence (ABC) Scale. *The journals of gerontology. Series A, Biological sciences and medical sciences* **50a**, M28-34 (1995).
100. Franchignoni, F., Giordano, A., Ronconi, G., Rabini, A. & Ferriero, G. Rasch validation of the Activities-specific Balance Confidence Scale and its short versions in patients with Parkinson's disease. *J Rehabil Med* **46**, 532-539 (2014).